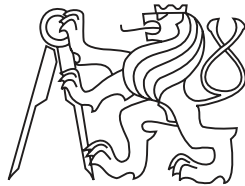


České vysoké učení technické v Praze
Fakulta jaderná a fyzikálně inženýrská

Katedra fyziky
Obor: Experimentální jaderná a částicová fyzika



Charakterizace křemíkového senzoru ALPIDE

Characterization of the ALPIDE silicon sensor

Diplomová práce

Vypracovala: Bc. Valentina Raskina
Vedoucí práce: RNDr. Filip Křížek, Ph.D.
Školitel specialista: Svetlana Kushpil, CSc.
Rok: 2020

Název práce:

Charakterizace křemíkového senzoru ALPIDE

Autor: Bc. Valentina Raskina

Obor: Experimentální jaderná a částicová fyzika

Druh práce: Diplomová práce

Vedoucí práce: RNDr. Filip Křížek, Ph.D.
Ústav jaderné fyziky AV ČR, v.v.i.

Konzultant: Svetlana Kushpil, CSc.
Ústav jaderné fyziky AV ČR, v.v.i.

Abstrakt: Experiment ALICE v CERN připravuje inovaci svého vnitřního dráhového detektoru. Tento detektor bude sestávat ze sedmi koncentrických vrstev křemíkových senzorů ALPIDE založených na technologii MAPS. S tímto projektem je spojena celá řada testovacích studií, kdy se sleduje odezva senzorů ALPIDE na částice ionizujícího záření. K testování radiační odolnosti senzorů používáme cyklotron U-120M, který se nachází v Ústavu jaderné fyziky AV ČR v Řeži. Hlavním cílem této práce je vyhodnotit výsledky radiačních testů senzoru ALPIDE prováděných na cyklotronu U-120M.

Klíčová slova: ALICE ITS upgrade, polovodičové detektory, radiační poškození v polovodičových detektorech, ALPIDE, MAPS, cyklotron

Title:

Characterization of the ALPIDE silicon sensor

Author: Bc. Valentina Raskina

Abstract: The experiment ALICE at CERN plans to upgrade its Inner Tracking System detector. This detector will consist of seven concentric cylindrical layers of silicon sensors ALPIDE based on the MAPS technology. This project encompasses a wide range of tests which characterize response of ALPIDE sensors to ionization radiation. For radiation hardness tests of this sensor, the cyclotron U-120M of the Nuclear Physics Institute of the Czech Academy of Sciences in Řež is used. The main goal of this thesis is to analyse the results of radiation hardness tests of ALPIDE sensors carried out at the cyclotron U-120M and make a subsequent characterization of the chip.

Key words: ALICE ITS upgrade, semiconductor detectors, radiation damage in semiconductors, ALPIDE, MAPS, cyclotron

Contents

Introduction	11
1 Semiconductor detectors	14
1.1 Effect of Impurities or Dopants	16
1.1.1 p-type semiconductors	16
1.1.2 n-type semiconductors	17
1.2 The pn - Junction	18
1.2.1 Position sensitive semiconductor detectors	19
1.3 Signal generation in silicon sensors	20
1.4 Radiation damage in semiconductors	21
1.4.1 Effects of radiation damages in semiconductor detectors . .	22
2 ALICE ITS upgrade	24
2.1 ITS upgrade	24
2.2 The ALPIDE chip	26
3 Experimental Setup for radiation hardness tests of ALPIDE	31
3.1 Cyclotron U-120M	31
3.2 Ionization chamber PTW 30010 Freiburg	35

3.3	Setup for irradiation tests at the U-120M cyclotron	36
3.4	The irradiation process	39
4	Analysis of radiation hardness tests at the U-120M cyclotron	43
4.1	Estimate of NIEL induced by secondary neutrons	47
4.2	The analysis of threshold and temporal noise	51
4.3	The analysis of I_{THR} and V_{CASN}	57
4.4	Fake-hit rate	64
4.5	Characterization of the irradiated chip	70
4.5.1	The setup for the CERN PS test beam	71
5	ALICE ITS Commissioning	76
	Conclusion	79
	Literature	80
	Appendix	83
A	Dose calculation	84

Prohlášení

Prohlašuji, že jsem svoji diplomovou práci vypracovala samostatně a použila jsem pouze podklady (literaturu, projekty, SW atd.) uvedené v příloženém seznamu.

Nemám závažný důvod proti použití tohoto školního díla ve smyslu §60 Zákona č. 121/2000 Sb., o právu autorském, o právech souvisejících s právem autorským a o změně některých zákonů (autorský zákon).

V Praze dne

.....
Bc. Valentina Raskina

Acknowledgment

I would like to express my sincere gratitude to my supervisor, RNDr. Filip Křížek, Ph.D., for his patient guidance, great support, encouragement, invaluable advices and his time. I wish to express my sincere thanks to my beloved family for their endless support and love. Acknowledgments also go to Ing. Artem Isakov and Svetlana Kushpil, CSc. for their help.

Bc. Valentina Raskina

Introduction

ALICE (A Large Ion Collider Experiment) [1] is a heavy-ion detector at the CERN Large Hadron Collider (LHC) [2]. It is designed to study strongly interacting matter in the regime of high-energy densities and temperatures using proton-proton, proton-nucleus and nucleus-nucleus collisions. In this regime, nuclear matter undergoes a transition to the state called Quark-gluon plasma (QGP) [3], consisting of deconfined color charge particles, quarks and gluons [4, 5]. Information about QGP properties can be obtained indirectly, e.g. from measurements of particle multiplicities, transverse momentum spectra, azimuthal distribution of particles with respect to reaction plane and from jet quenching measurements [5, 6]. The multiplicity of final state particles created in a heavy-ion collision is high and can reach a couple of thousands of particles per unit of pseudorapidity in midrapidity [7]. ALICE was therefore designed as a multipurpose detector which is able to provide efficient track reconstruction and particle identification in a high-multiplicity environment. The ALICE detector consists of a central barrel, a forward muon spectrometer, and a set of small detectors for triggering and event characterization. ALICE allows studying hadrons, electrons, muons, photons and jets. The schematic drawing of the current ALICE detector is shown in Figure 1.

Run3 and Run4 are the new periods of data taking after the Second Long LHC shutdown (LS2). The LS2 will take place in 2019–2020 and is intended for the LHC upgrade. ALICE expects that in Run3 + Run4, the LHC will deliver 100 times higher luminosity with respect to previous data taking periods. To be able to accomplish the physics program planned for Run3 + Run4, ALICE will undergo an upgrade during the LS2 [8]. The main goals of the ALICE physics program for Run3 + Run4 are summarized in the letter of intent from 2014 [9]. ALICE wants to:

- measure open heavy flavor (HF) hadrons and quarkonia down to zero p_T to gain more information about HF thermalization and temperature evolution of the QGP,
- measure vector mesons and low-mass di-electrons which carry information about chiral symmetry restoration and thermal radiation from the QGP,
- perform high-precision measurements of the light nuclei, anti-nuclei, and hyper-nuclei production.

Since none of these observables provides a suitable trigger signature, ALICE plans to take minimum bias events in a continuous readout mode. The ALICE upgrade can be described as follows. Starting from the center of ALICE, there will be a new silicon Inner Tracking System (ITS), see Figure 2. In front of the muon arm absorber, there will be a new forward muon tracker with five layers of silicon sensors which will improve resolution in the muon arm. The Time Projection Chamber (TPC) will upgrade its readout system to allow continuous readout, the gating grid in the TPC will be replaced with a stack of GEM foils. They will provide electron multiplication and prevent the backward flow of positive ions back to the TPC [10]. The current forward detectors T0 and V0 which are used for centrality selection, event plane reconstruction and triggering will be replaced by a new Forward Interaction Trigger (FIT) detector [11]. Other detector upgrades concern readout electronics.

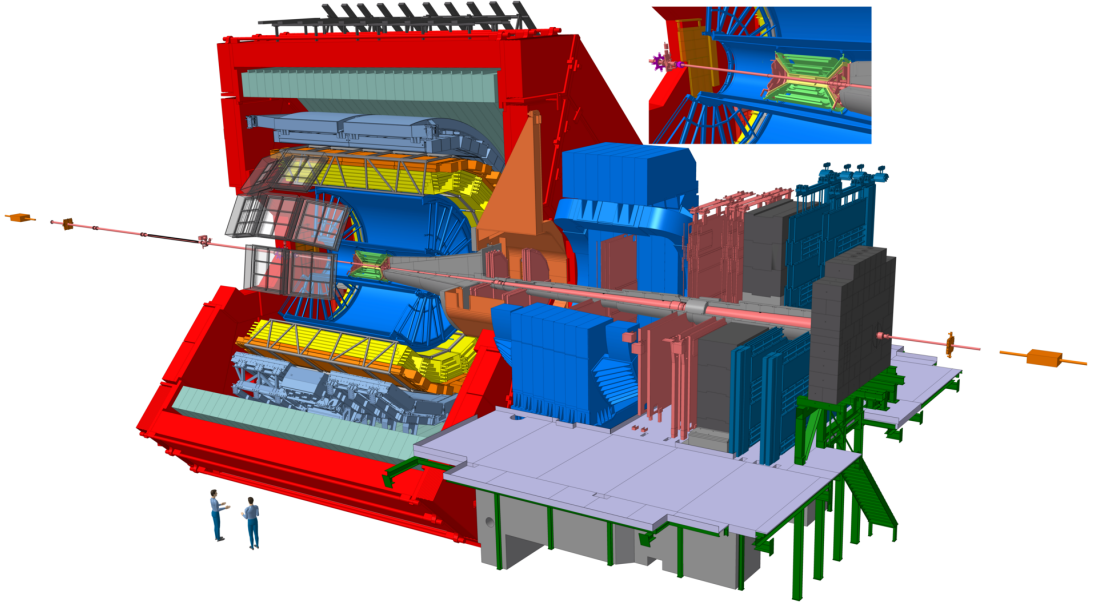


Figure 1: The current ALICE detector, taken from [12]. ALICE consists of the central barrel and muon spectrometer. The current ITS is in the center of the central barrel and is colored green. Its zoomed sketch is in the upper right corner. The ITS is surrounded by the TPC detector, colored blue. The red part of the detector is a solenoid, which creates a magnetic field of 0.5 T

This work is related to the upgrade of the ITS. In particular, it deals with radiation hardness tests of ITS pixel sensor ALPIDE and its characterization. The new ALICE ITS will consist of seven concentric cylindrical layers of ALPIDE chips, 4 layers in the Outer Barrel (OB) and 3 layers in the Inner Barrel (IB). The expected Total Ionization Dose (TID) that an IB sensor will get during Run3 + Run4 is 270 krad and the expected Non-Ionizing Energy Loss (NIEL) is $1.7 \times 10^{12} \text{ 1 MeV n}_{\text{eq}} \text{ cm}^{-2}$ [13]. The project goal, however, assumes that the ALPIDE chip should sustain ten times higher radiation loads [8].

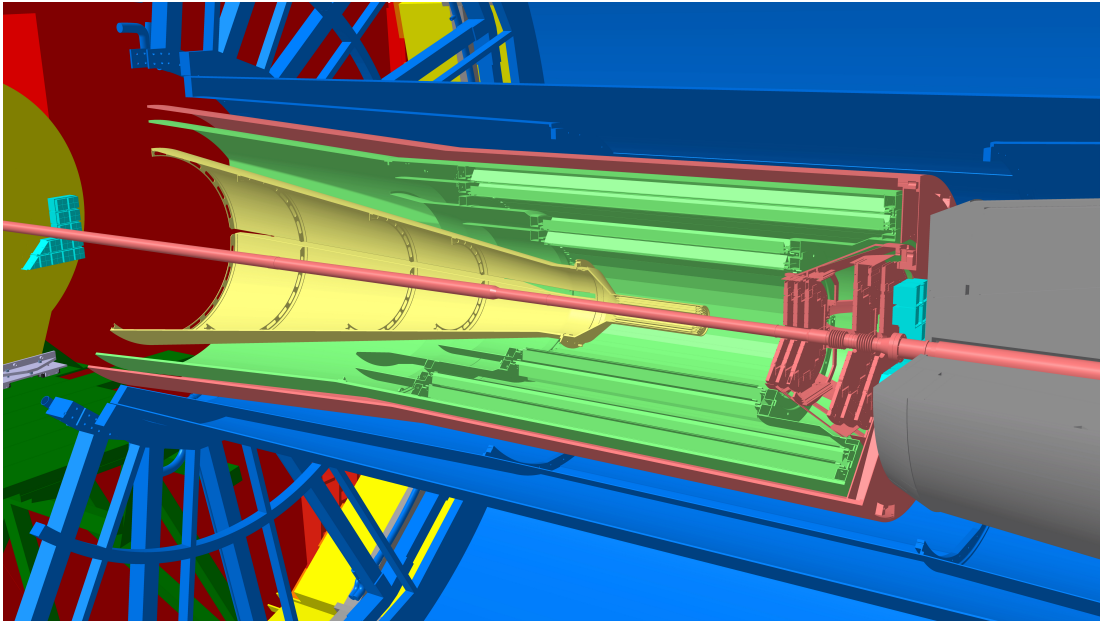


Figure 2: Central part of the ALICE detector after the upgrade, taken from [12]. The new ITS is colored green and yellow. The MFT is colored pink, the FIT is light blue and it is installed on the left-hand side and right-hand side of the ITS.

The first goal of this thesis is to investigate radiation hardness of the ALPIDE sensor using the 30 MeV proton beam provided by the U-120M cyclotron of the Nuclear Physics Institute of the Czech Academy of Sciences in Řež. The second goal is to analyze data from ALPIDE beam tests done at the CERN Proton Synchrotron (PS).

This research work is organized as follows. Chapter 1 gives a brief introduction to semiconductor detectors and the problematics of their radiation damage. Chapter 2 describes the upgraded ITS and the ALPIDE sensor. The third chapter is dedicated to experimental setup for radiation hardness tests of ALPIDE sensors at the U-120M cyclotron in Řež. The final chapter presents the analysis of irradiations at the U-120M cyclotron and the CERN PS.

Chapter 1

Semiconductor detectors

Semiconductor detectors are solid-state detectors, based on a crystalline semiconductor material. The most commonly used semiconductor materials are silicon (Si), germanium (Ge), gallium arsenide (GaAs) or cadmium-zinc-telluride (CdZnTe). The operating principle of semiconductor detectors is that ionizing radiation passing through the sensitive area of a detector (semiconductor) creates electron-hole pairs that can be moved and collected by an electric field. The energy needed to create an electron-hole pair in a semiconductor material is very small, e.g. 3.6 eV for Si [14], which is a primary advantage of semiconductors when compared to a gas detector where the ionization energy is an order of magnitude higher. Further advantages of semiconductor detectors with respect to gas detectors can be listed as follows [15]

- high density of semiconductors, which allows achieving large energy loss per traversed distance and allows to make the detector thin,
- high mobility μ of charge carriers (in silicon μ of electrons is $\approx 1400 \text{ cm}^2 \cdot \text{V}^{-1} \cdot \text{s}^{-1}$ and μ of holes is $\approx 450 \text{ cm}^2 \cdot \text{V}^{-1} \cdot \text{s}^{-1}$ [16]),
- excellent mechanical rigidity,
- possibility to integrate sensitive volume and signal processing circuits [15].

In order to have a better understanding of semiconductor detectors, let us briefly remind the basics of the Band theory [17], which describes the energy spectrum of electron levels in a lattice. Quantum mechanics predicts that discrete electron energy levels of isolated atoms evolve into energy bands once the atoms are placed close to each other on a crystalline lattice. In the energy band, the electron levels are so close to each other that electrons can move from one to another level. Such transition between levels requires minimum energy, which can be obtained, for example, by thermal motion. The allowed energy bands are the valence band and conduction band.

In different materials, energy bands have different relative positions. There are three groups of materials according to the configuration of bands: insulators, conductors and semiconductors [17], see Fig. 1.1. Insulators have a width of the forbidden band larger than 2 eV. Conductors do not have the forbidden band. Semiconductors are characterized by a band structure where the valence band and the conduction band are separated by a narrow forbidden band. In semiconductors, the width of the forbidden band is less than 2 eV [14], so even small thermal excitations can provide sufficient energy to electrons to overcome the bandgap. For example, the forbidden band of silicon with temperature 273 K is about 1.1 eV [14]. Let us also point out that silicon is an indirect semiconductor which means that electron states in the conductive and the valence band have different momenta [15].

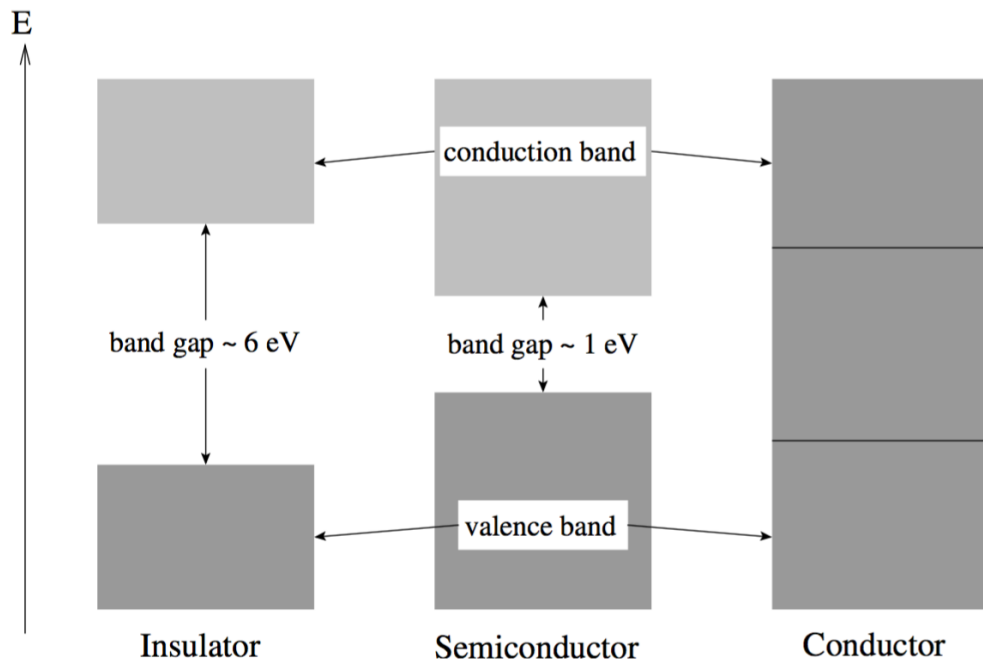


Figure 1.1: Energy band diagrams for insulator, semiconductor and conductor, taken from [17].

Excitation of an electron in the valence band of a semiconductor leads to creation of a hole in the valence band and a free electron in the conduction band. A combination of these charges is called an *electron – hole pair*. If an electric field is applied to the semiconductor, free electrons and holes start to move in opposite directions. The probability that a free electron will have energy E is given by the Fermi function $f(E)$ [17]:

$$f(E) = \frac{1}{1 + e^{(E-E_F)/kT}}, \quad (1.1)$$

where k is the Boltzmann constant, T is the temperature, E_F is the Fermi level, which is the energy level which electrons occupy with the 50% probability. By

integrating the Fermi function and carrier concentration, we get the density of free electrons n [17]:

$$n = 2 \left(\frac{2\pi m_n kT}{h^2} \right)^{\frac{3}{2}} e^{-\frac{E_C - E_F}{kT}} = N_C e^{-\frac{E_C - E_F}{kT}}. \quad (1.2)$$

Similarly for the density p of free holes we obtain:

$$p = 2 \left(\frac{2\pi m_p kT}{h^2} \right)^{\frac{3}{2}} e^{-\frac{E_F - E_V}{kT}} = N_V e^{-\frac{E_F - E_V}{kT}}. \quad (1.3)$$

Here m_n is an effective electron mass, m_p is an effective hole mass, h is the Planck constant, T is the absolute temperature, E_C is a conduction energy level, E_V is a valence energy level, E_F denotes Fermi energy level and N_C and N_V are the effective densities of states in the conduction and valence bands.

In a pure semiconductor with no impurities, electron-hole pairs are produced by thermal excitation (without ionizing radiation), each excited electron leaves the hole behind, so the number of electrons in the conduction band and holes in the valence band is equal:

$$p = n = n_i, \quad (1.4)$$

where n_i is the intrinsic concentration [15]. Such materials are called ideal semiconductors or *intrinsic* [17].

Ideal semiconductor, however, does not exist in nature. Crystal impurities and defects imply additional energy levels within the forbidden band, which change the conductive properties of the material. Then the electron and hole densities do not have to be in equilibrium. In general, any adding of impurity causes a change of conduction properties of a material. Material with added impurities is called *extrinsic* semiconductor and the process, which leads to its creation, is called *doping*. The impurity that causes an increase of the number of holes in a semiconductor is called *acceptor* impurity and the impurity that increases the density of electrons is the *donor* impurity [17]. Generally, the small density of impurities is needed for semiconductors used as a radiation detector. For example in silicon-based semiconductors for each impurity atom, there are $\approx 10^{10}$ atoms of Si. When density of majority carriers (in the case of n - type semiconductor carriers are electrons) increases, the density of minority carriers decreases [15]:

$$n \cdot p = n_i^2. \quad (1.5)$$

1.1 Effect of Impurities or Dopants

1.1.1 p-type semiconductors

If the impurity added in a semiconductor has fewer valence electrons than the initial semiconductor elements, it will capture a valence electron from a neigh-

boron atom and form less bonds than a semiconductor atom does. This will also create extra holes in an extrinsic semiconductor. Such materials are known as p-type semiconductors. These semiconductors have additional acceptor type energy levels near the valence band. For example, by adding boron in silicon, one will obtain acceptor level with energy $E_A = E_V + 0.045 \text{ eV}$ [15], where E_V is the valence band energy, see Fig. 1.2 left. Because 0.045 eV is small energy, even thermal energy can overcome it, so that the impurity atom will be ionized. In Fig. 1.2right, the acceptor doping of silicon by boron is shown.

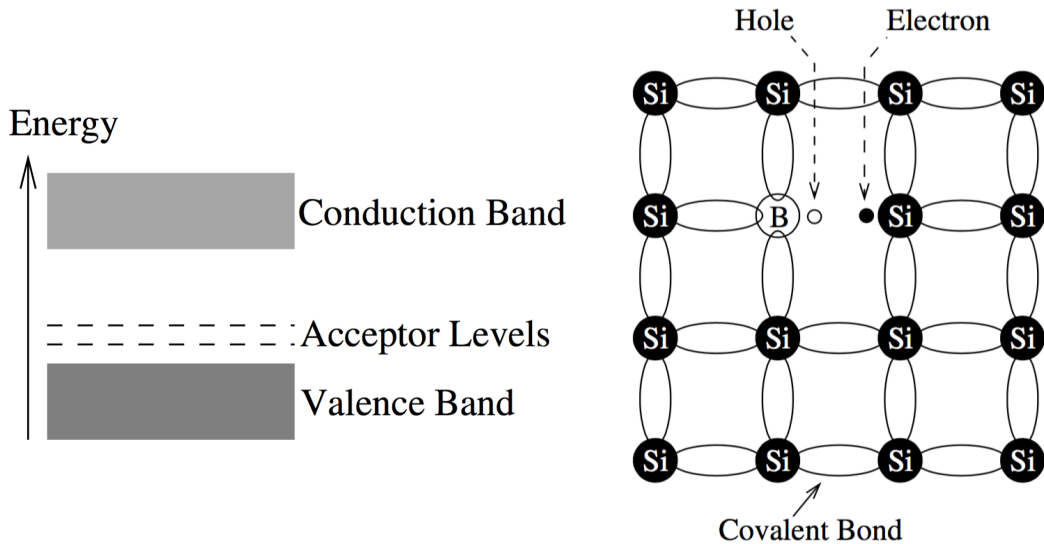


Figure 1.2: Left: energy band diagram with acceptor levels, [17]. Right: doping of Si lattice by boron. Since boron has one electron less, it can form only 3 covalent bonds with neighboring silicon atoms. The fourth unfilled band behaves as a hole since it attracts free electrons. If this hole is filled by a neighboring electron, it will appear at the initial place of this electron. [17].

1.1.2 n-type semiconductors

If the impurity element has more valence electrons than the semiconductor atoms, the extra electrons are not able to make covalent bonds with semiconductor atoms, so they are free. Such a semiconductor material with a donor impurity is called an n-type semiconductor. Doping with donor impurity creates new donor type energy levels near to the conduction band. Similarly as in p-type semiconductors, phosphorus in silicon makes a donor level with energy $E_D = E_C - 0.054 \text{ eV}$ [15], where E_C is the conduction band energy, see Fig 1.3 left. These extra levels cause that the forbidden gap is effectively reduced, which improves the conduction properties of the material. In Fig. 1.3 right, the donor doping of silicon by phosphorus is shown.

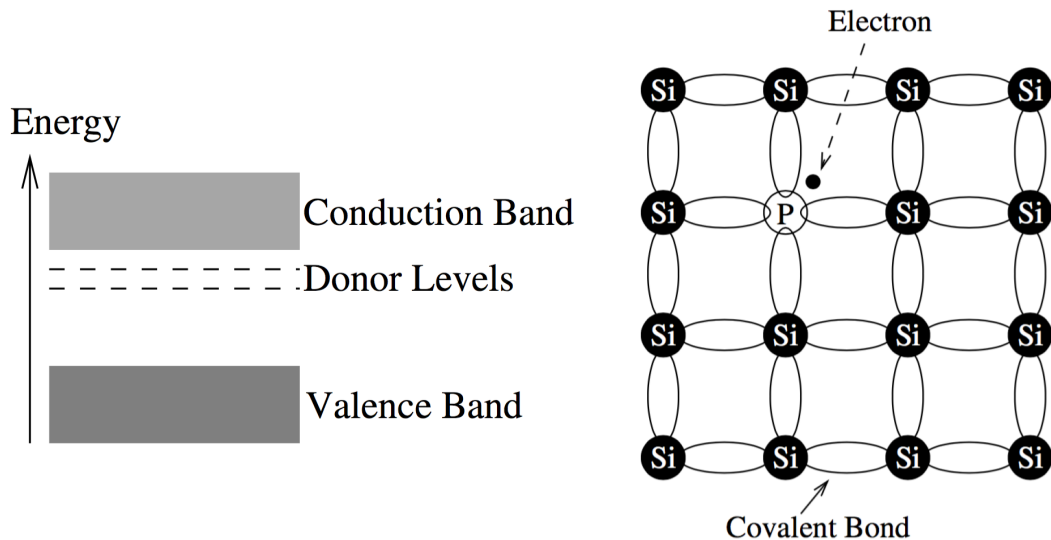


Figure 1.3: Left: energy band diagram with donor levels, [17]. Right: doping of Si lattice by a phosphorus atom. Since phosphorus atom has 5 available electrons for bonding, but since silicon has only 4 valence electrons, one extra electron from phosphorus outer shell becomes free, [17].

1.2 The pn - Junction

The basis of all semiconductor detectors is the so-called pn-junction, which is obtained by joining together n-type and p-type semiconductors. When a p- and n-type semiconductors are brought together, electrons will diffuse into the p region and holes into the n region to compensate the imbalance across the junction. As a result of the diffusion and recombination process, the concentration of negative charge will decrease at the border of the n region, which will become positive. Similarly, at the border of the p region, the concentration of holes will decrease, so this region will become negative. In this way, an electric field will be created, which counteracts the further diffusion, creating a depletion zone (a region free of mobile carriers) with a potential between p- and n- region, the so-called built-in voltage V_{bi} , see Fig. 1.4:

$$V_{bi} = \frac{kT}{q} \ln \left(\frac{N_d N_a}{n_i^2} \right), \quad (1.6)$$

where N_d and N_a are donor and acceptor concentrations on the n and p sides, q is the unit elementary charge [18]. The depletion zone is sensitive in semiconductor detectors, where the incident radiation creates electron-hole pairs. The external electric field makes charges moving. The created current causes associated voltage drop, which can be measured. However, the junction is too thin for effective radiation detection and the potential is also small. The width of the depletion region can be regulated by applying an external voltage. Applying positive potential to the p-region and negative to the n-region, the potential barrier reduces and the current across the junction increases. When the opposite polarity is applied (back bias), the potential barrier increases and the width of the depletion grows, this regime is used in detectors.

The width of the depletion zone w with applied external back bias V_{bb} is given by:

$$w = \sqrt{\frac{2\epsilon}{e} \frac{N_a + N_d}{N_a N_d} (V_{bi} - V_{bb})}, \quad (1.7)$$

where ϵ is the dielectric constant, e is elementary charge [18].

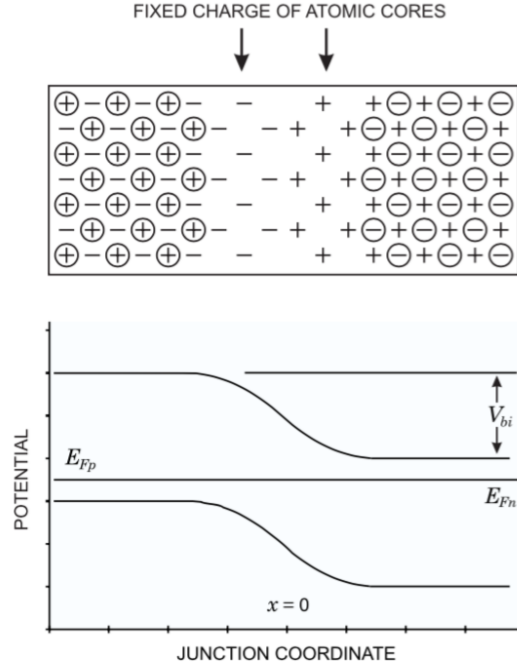


Figure 1.4: Diffusion of electrons and holes across the pn-junction forms a depletion zone with a built-in potential V_{bi} between the p- and n-regions, E_{Fn} and E_{Fp} are Fermi levels of n- and p-regions, [18].

1.2.1 Position sensitive semiconductor detectors

The silicon detectors have different structures and configurations: strip detectors, hybrid pixel detectors, Charged Coupled Devices (CCD), Silicon Drift Detector (SDD), Monolithic Active Pixel Sensors (MAPS) and other [15].

The current ALICE ITS innermost layers consist of hybrid pixel detectors [1]. In those detectors, the CMOS chip, which includes the front-end and the readout logic, and the sensitive layer are separated by fine pitch bump-bonding. This allows optimizing both parts separately. Furthermore by applying larger bias voltages, one may obtain the full depletion with larger electric fields, which leads to faster charge collection and higher efficiency [19]. However, hybrid pixel detectors can not fulfill the requirement of the new ITS to reduce the material budget. Moreover, they are complicated to construct and relatively expensive.

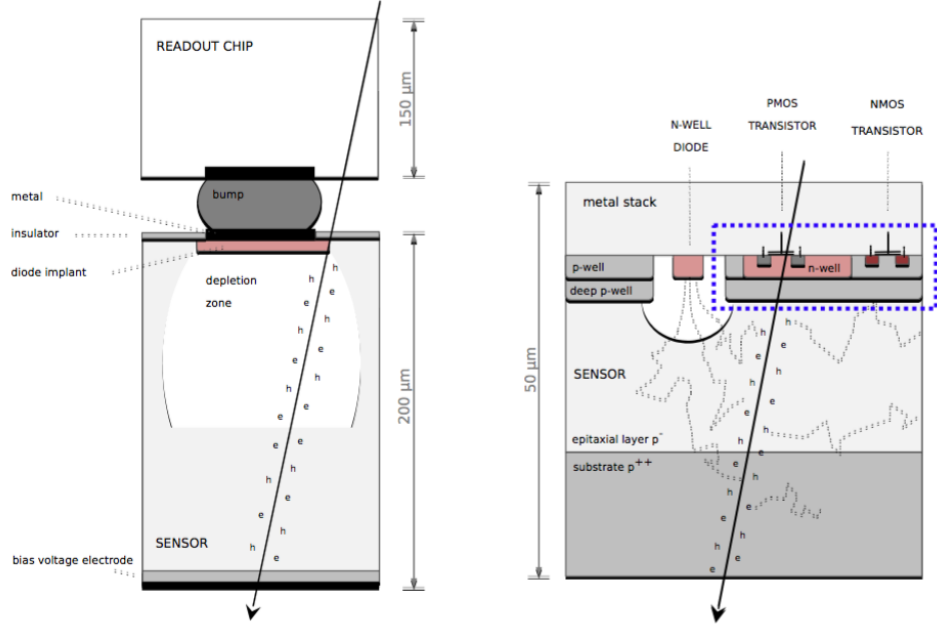


Figure 1.5: To the left: Hybrid pixel sensor, sensitive layer and front-end circuitry are separated by a bump bond [19]. To the right: MAPS. The front-end circuitry is located in the blue marked area [19].

Monolithic Active Pixel Sensors (MAPS) combine front-end circuitry and sensitive layer in one layer of silicon in comparison to hybrid pixel sensors, see Fig. 1.5, which allows reducing the material budget. The MAPS were first implemented in the STAR PXL detector at RHIC [20]. However, they were not used by ALICE in tracking systems because of the limited radiation tolerance and slow readout. For the ITS upgrade, ALICE adopted MAPS created by the TowerJazz 180 nm CMOS technology which is better suited to ALICE needs, see chapter 2.2.

1.3 Signal generation in silicon sensors

Charged particles crossing material deposit a part of their energy by means of scattering processes with electrons of the medium. The mean energy loss per unit traversed length is described by the Bethe-Bloch formula [14]:

$$\left\langle -\frac{dE}{dx} \right\rangle_{\text{ion}} = \frac{4\pi z^2 e^4}{m_e v^2} n \left[\ln \frac{2m_e v^2}{I_{\text{ion}}(1 - \beta^2)} - \beta^2 - \delta - U \right], \quad (1.8)$$

where z is the particle charge, v is the particle velocity, c is the speed of light in vacuum, $\beta = \frac{v}{c}$, n is the density of electrons in the material, I_{ion} - excitation energy of atom, δ - correction for material density and U is correction for binding

energy of electrons on orbitals K, L and others. The energy loss depends on the path length of the particle in the material and is minimal for particles with $\beta\gamma \approx 3 - 4$ (Minimum Ionizing Particles).

The charge collection mechanism of MAPS detectors is the following. Generated free charge carriers diffuse across the epitaxial layer, which is not fully depleted, until reaching the drift region of an n-well diode, where they are collected. The measured voltage drop V is given by the diode capacitance C and the collected charge Q :

$$\Delta V = \frac{Q}{C}. \quad (1.9)$$

If the capacitance is small, then even a small collected charge is enough for high ΔV .

1.4 Radiation damage in semiconductors

The performance of a semiconductor detector depends on its radiation hardness. Radiation can cause serious lattice damage, which can affect the efficiency of charge collection inside of the semiconductor detector [18]. The overall damage depends on instantaneous and integrated doses. Radiation can affect the semiconductor by two basic mechanisms:

- **Displacement of material atoms**, which destroys lattice structure. This damage is quantified by the Non-Ionizing Energy Loss (NIEL) scaling [18], which allows comparing the damages caused by different radiations. Such defects can be scattered or clustered around the particle trajectory. The isolated atomic displacements away from each other are called point defects. A cluster of atomic displacements close to each other is called a cluster defect. The primary knocked-on atom (PKA) moved by NIEL from its initial site can cause further damage, which is not a part of NIEL. In contrary to ionizing energy loss, NIEL is not proportional to absorbed energy, but it depends on the type of radiation and particle energy. NIEL damage caused by an incident particle with energy E is given by:

$$D(E) = \sum_i \sigma_i(E) \int_0^{E_{R,max}} f_i(E, E_R) P(E_R) dE_R, \quad (1.10)$$

where $\sigma_i(E)$ is a cross-section of the i -th interaction, $f_i(E, E_R)$ is a probability of generation of a PKA (Primary Knock-On Atom), E_R is a recoil energy and $P(E_R)$ is a fraction of energy that goes into the displacement of a silicon atom [21], $D(E)$ is calculated over all possible interactions. In Fig. 1.6, the dependence of NIEL damage function on the energy of the initial particle for different particles is shown. Usually, NIEL values are normalized and expressed in terms of 1 MeV neutron equivalent [15]. For

example protons with the kinetic energy 30 MeV used in the radiation hardness tests presented in this work have the $D(E)/95 \text{ MeV}\cdot\text{mb} \approx 2$. I.e. they cause about twice larger NIEL than 1 MeV neutrons.

- **Ionization damage** basically affects the surface and insulating SiO_2 layers of the sensor. This damage is called the total ionizing dose (TID). Ionizing radiation creates electron-hole pairs in the oxide layer. Because electrons have high mobility in the oxide, they are collected by the nearest positively biased electrode. As holes have low mobility and move very slowly in the direction of the electric field, they may be captured by the interface trap. This leads to the change of circuit operation. Ionization effects strongly depend on the absorbed energy and are independent of the type of radiation [18].

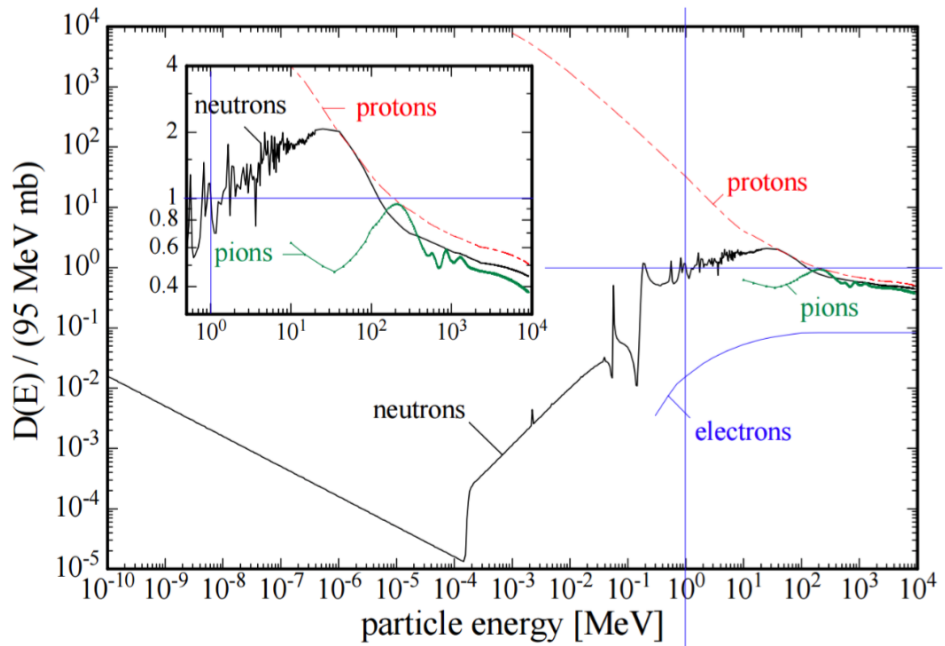


Figure 1.6: Damage function normalized to $95 \text{ MeV}\cdot\text{mb}$ for neutrons, electrons, protons and pions. The value 95 MeV corresponds to the NIEL of $1 \text{ MeV } n_{\text{eq}}$ [22].

1.4.1 Effects of radiation damages in semiconductor detectors

Properties of semiconductor detectors can change under the influence of radiation effects [17]. The most considerable are the following.

- **Increase of leakage current and charge trapping.** The radiation-induced lattice defects make traps, which capture charge and liberate it very slowly.

This charge contributes to the reverse bias current across the depletion region. The increase of leakage current has unwanted consequences on detector performance, for example, an increase in noise. Those traps may also function as recombination centers, which decrease detector efficiency. Moreover, some lattice defects can add extra energy levels to the band structure, making thermal excitations of electrons to the conductive band more probable, which also increases noise. Fortunately, the strong dependence on temperature can be exploited to compensate for the deterioration by decreasing the operating temperature.

- **Type Inversion.** Radiation may also affect impurity atoms, which may lose their function as acceptor or donor, becoming electrically inactive. Furthermore, this can lead to the inversion of the material type, when an n-type material may change into a p-type and the other way round after prolonged irradiation. This effect can be explained by the fact that radiation damage can change the effective dopant concentration in the material by increasing the charge carriers of the opposite sign. With an increasing integrated radiation dose, the original dopant concentration may be overcome by the opposite charges.

Radiation damage is to some extent repaired by the annealing process. This is a healing process, during which the radiation damage accumulated by detector decreases with time. Annealing process strongly depends on temperature. The defect concentration $N(t)$ can be parameterized as follows:

$$N(t) = N_0 e^{-t/\tau}, \quad (1.11)$$

where N_0 represents the initial defect concentration and τ is a function of the activation energy E_a and absolute temperature T :

$$\tau = A e^{E_a/kT}. \quad (1.12)$$

Here k is the Boltzmann's constant and A is an experimentally obtained value [17].

Chapter 2

ALICE ITS upgrade

2.1 ITS upgrade

In this section, we will discuss the key features of the ITS upgrade, see Fig. 2.1. The main goals of the ITS upgrade are: to improve impact parameter resolution of reconstructed tracks, to improve tracking efficiency and p_T resolution at low p_T , to increase readout rate and to allow fast insertion and removal of the detector during the end of year technical stops. A comparison of the current ITS performance and the upgraded ITS performance is shown in Fig. 2.2. Detailed discussion of the new ITS can be found in [8], here we will highlight the basic improvements of the ITS:

- **Shifting the first detection layer closer to the beam line.** The reduction of the beam pipe diameter in the centre of the ALICE detector is one of the main points which will help to improve the impact parameter resolution. The current beam pipe with radius 29 mm will be replaced by a beryllium beam pipe having a radius of 17.2 mm. The wall thickness of the beam pipe is assumed to be 0.8 mm. The innermost detector layer can thus be moved closer to the interaction point from the current 39 mm to 23 mm.
- **Geometry and segmentation.** The baseline solution for the layout of the ITS upgrade is to replace six cylindrical layers of silicon pixel, drift and strip detectors with seven concentric cylindrical layers covering a radial extension from 22 mm to 430 mm with respect to the beam line. The upgraded ITS will cover the pseudo-rapidity range of $|\eta| < 1.22$ for 90% of the most luminous beam interaction region.
- **Reduction of material budget.** This will allow the tracking performance and momentum resolution to be significantly improved. The MAPS, which will be used will allow to reduce material budget per layer in comparison to the present ITS (50 μm per layer in IB instead of 350 μm). The pixel density will be increased by a factor of ≈ 24 . The pixel size will be reduced from 50 $\mu\text{m} \times 425 \mu\text{m}$ to 29.24 $\mu\text{m} \times 26.88 \mu\text{m}$. The area covered by MAPS will be 10 m^2 . In total, there will be 24 000 sensors.

- **Readout time.** The present ITS has a maximum readout rate of 1 kHz. The new detector is designed to be able to read the data in a continuous readout or a triggered mode up to a rate of 100 kHz for Pb–Pb collisions and 400 kHz for pp collisions.
- **Fast insertion removal.** The rapid accessibility to the detector for maintenance and repair interventions during the yearly LHC shut-downs will also be provided.

The characteristics listed above will enable the track position resolution at the primary vertex to be improved by a factor of 3 or larger. In the next section, we give more details about the pixel sensors that will be used in the new ITS.

As was already mentioned above, the upgraded ITS will consist of three innermost layers (composing an IB) and four outermost layers (composing an OB) which are azimuthally segmented in so-called Staves. Staves are maintained to the support systems that form the Half-Layers (shape of a half-wheel). Each stave contains a Flexible Printed Circuit (FPC) to which pixel chips (9 for IB and 14 for OB) are glued and wire-bonded, a Cold Plate and a Space Frame. The OB layer consists of the 2 middle layers (ML) and the two outer layers (OL). Each OB stave is divided azimuthally into the two so-called Half-Staves which are additionally longitudinally segmented into the modules. The detailed geometric characteristics of the detector are presented in the Tab. 2.1.

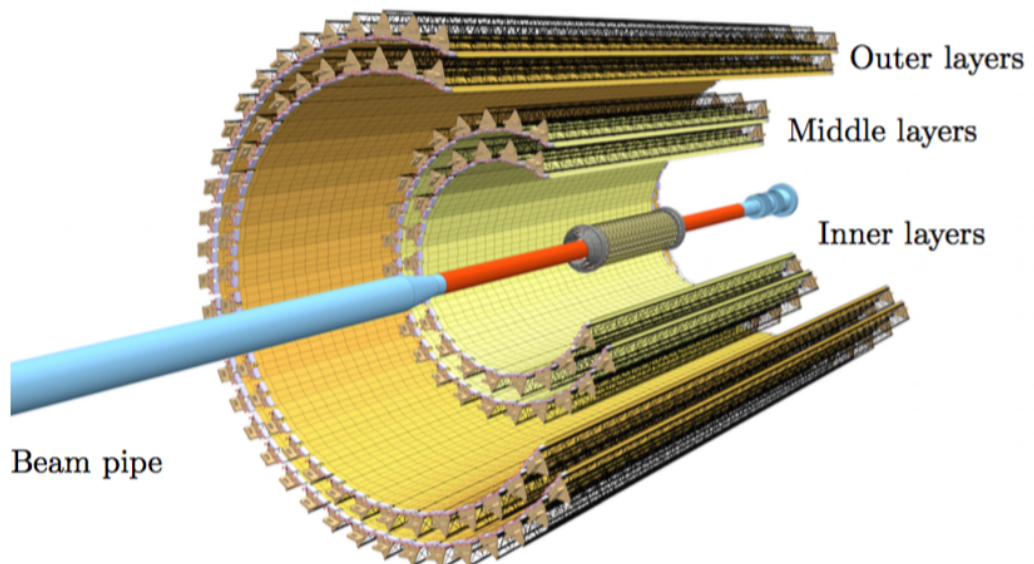


Figure 2.1: Layout of the upgraded ITS, taken from [8].

Barrel	Layers	Radius [cm]	Length [cm]	# Staves	# Chips
Inner	Layer 0	22.4	271	12	108
Inner	Layer 1	30.1	271	16	144
Inner	Layer 2	37.8	271	20	180
Outer	Layer 3	194.4	843	24	2688
Outer	Layer 4	243.9	843	30	3360
Outer	Layer 5	342.3	1475	42	8232
Outer	Layer 6	391.8	1475	48	9408

Table 2.1: The ITS layers geometric characteristics [8].

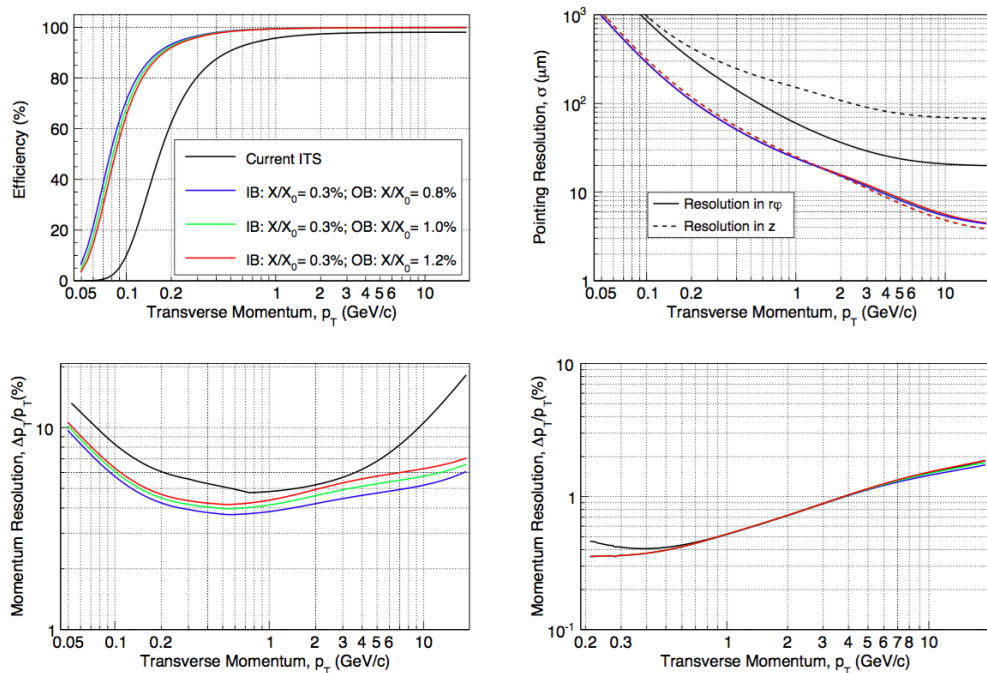


Figure 2.2: Top panels: Tracking efficiency (left) and pointing resolution (right) for charged pions vs. transverse momentum for the current ITS and the upgraded ITS design with different material budget options. Bottom panels: transverse momentum (p_T) resolution for charged pions vs. p_T for the current ITS and the upgraded ITS design with different material budget options (the results for the ITS stand-alone and ITS+TPC combined tracking are shown on the left and on the right, respectively). Taken from [1].

2.2 The ALPIDE chip

ALPIDE, which stands for ALICE P*IX*el D*E*tector [8], is a MAPS, see Section 1.2.1. The sensor has a size of $1.5 \text{ cm} \times 3 \text{ cm}$. It is divided into 512 rows and 1024 columns of pixels with a pitch of $29.24 \mu\text{m} \times 26.88 \mu\text{m}$. The current version of ALPIDE is a result of several year long process of research

and development, during which several sensor prototypes were designed and tested [19, 23]. Table 2.2 shows the parameters of ALPIDE, it is seen that performance of the sensor satisfies all Inner and Outer Barrel requirements as specified in the project proposal [8].

The ALPIDE uses the 180 nm CMOS technology of TowerJazz, see Fig. 2.3. This technology uses up to 6 metal layers which in combination with a small size of pixel implements high density and low power digital circuits. TowerJazz also allows to use a high-resistivity epitaxial layer and a deep p-well, see Fig. 2.4. The thickness of the sensitive layer is 18 – 30 μm . The deep p-well layer prevents the collection of charge carriers by the n-well of PMOS transistors that would compete with the n-wells collection diode. This process feature, together with six metal layers, allows to use both PMOS and NMOS transistors for the implementation of complex CMOS circuits in the active sensor area. A moderate bias voltage can be applied to the substrate, increasing the volume of the drift region around the n-well collection diode and reducing its capacitance.

	Inner Barrel	Outer Barrel	ALPIDE performance
Thickness [μm]	50	100	OK
Spatial resolution [μm]	5	10	~ 5
Chip dimension [mm]	15×30	15×30	OK
Power density [mW/cm^2]	< 300	< 100	< 40
Event-time resolution [μs]	< 30	< 30	~ 2
Detection efficiency [%]	> 99	> 99	OK
Fake-hit rate [$\text{event}^{-1}\text{pixel}^{-1}$]	$< 10^{-6}$	$< 10^{-6}$	$< 10^{-10}$
NIEL radiation tolerance [$1 \text{ MeV } n_{\text{eq}}/\text{cm}^2$]	1.7×10^{13}	3×10^{10}	OK
TID radiation tolerance [krad]	2700	100	tested at 500

Table 2.2: IB and OB requirements, ALPIDE performance [23].

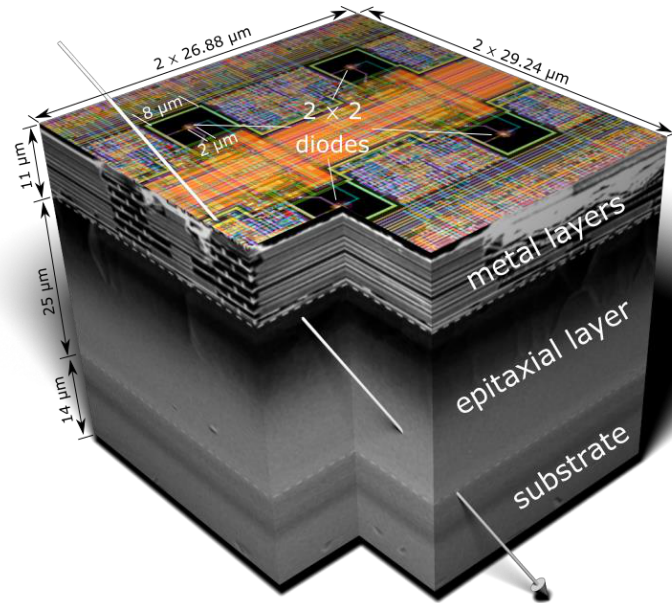


Figure 2.3: Sketch of a pixel of ALPIDE MAPS sensor with the TowerJazz technology, taken from [1].

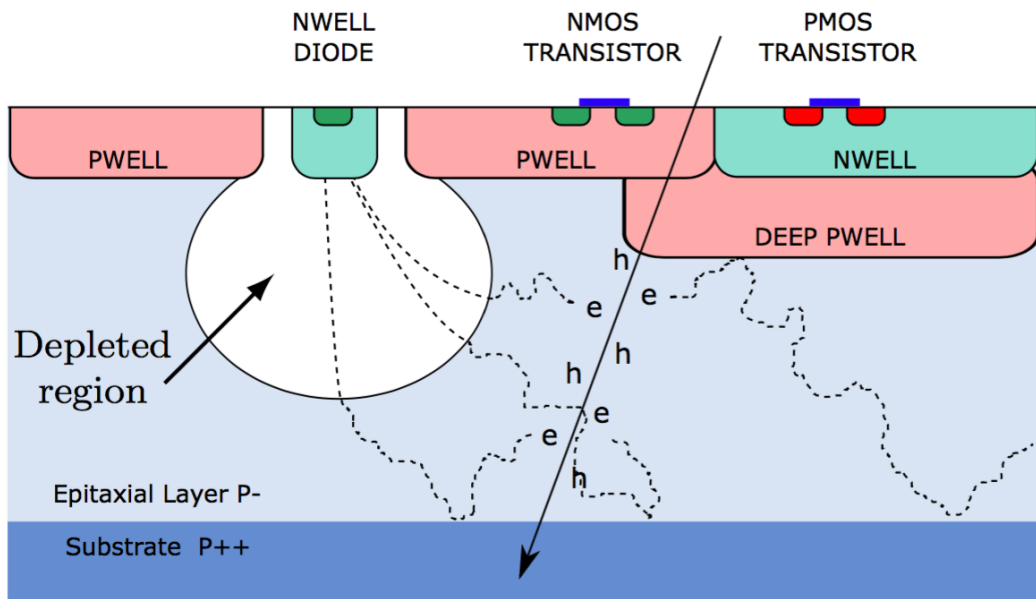


Figure 2.4: Schematic drawing of a pixel of ALPIDE MAPS sensor with the TowerJazz technology, taken from [1].

Each pixel of ALPIDE has an analog front-end circuit for signal amplification, hit discrimination and a 3 hit buffer [8]. First, charge is collected on the collection diode or injected through the capacitance C_{inj} . The generated current causes a voltage drop on the PIX_IN node, see Fig. 2.6. After that

the signal is amplified and discriminated with respect to the chosen threshold level. The binary signal is then sent to the in-pixel memory. The principle of charge amplification and discrimination can be understood from Fig. 2.7 where the in-pixel analog front-end is shown. The transistor M1 acting as a source follower forces the source voltage to follow the M1 gate voltage. The voltage drop at the PIX_IN node produces current between capacitances C_S and C_{OUT_A} resulting in a voltage gain. If there is a hit, the voltage at OUT_A node increases so the current through the M_8 gate increases. If this current will be larger than I_{DB} , there will be the discriminated signal at the OUT_D node, which is propagated to the in-pixel memory. The both voltage V_{CASN} and current I_{THR} define the baseline value of OUT_A node, when $I_{M8} < I_{DB}$. The charge threshold is defined by the distance of the OUT_A baseline voltage and the point when $I_{M8} = I_{DB}$. Increasing I_{THR} leads to the increase of the charge threshold, while increasing V_{CASN} reduces the threshold. In other words, charge threshold is influenced by two parameters: V_{CASN} and I_{THR} .

All the analog signals required by the front-ends are generated by a set of on-chip 8 bit DACs, which are implemented in chip, see Fig. 2.5. All of the voltages are beginning with V (V_{CASN} , V_{CASN2} , V_{CASP}) and currents with I (I_{THR} , I_{DB} , etc.).

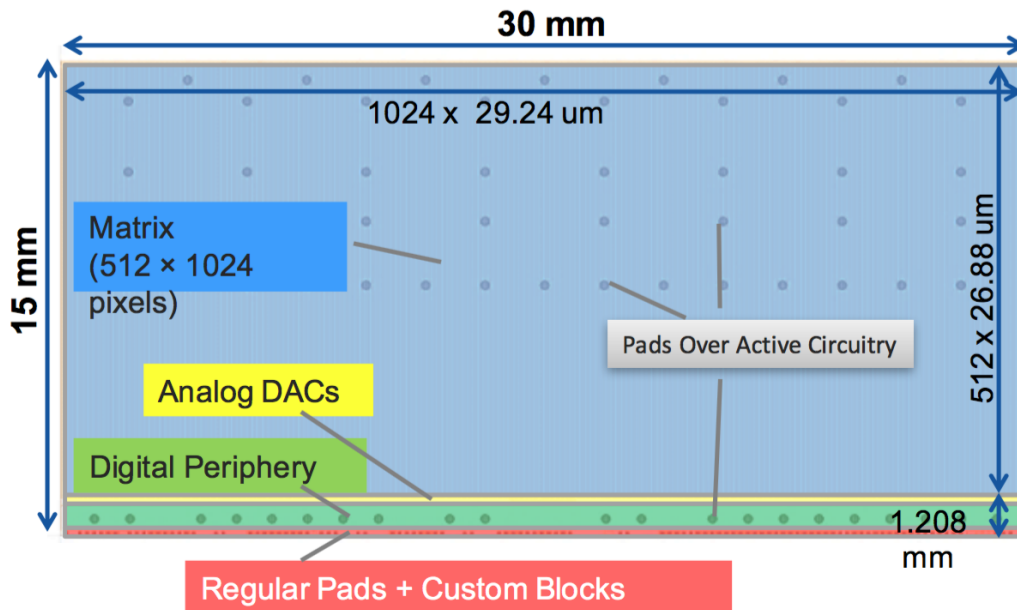


Figure 2.5: Scheme of the ALPIDE sensor with analog DACs in the bottom, taken from [24].

After the discrimination, the signal goes to the address decoder AERD (Address-Encoder Reset-Decoder) [25]. The address encoding of the hit pixels is provided by AERD logic. AERD is built as a tree structure. Each

element of the level represents 4 elements of underneath level, the lowest level is pixels level. The signal processing before the AERD logic is shown in Fig. 2.6. ALPIDE applies zero hit suppression.

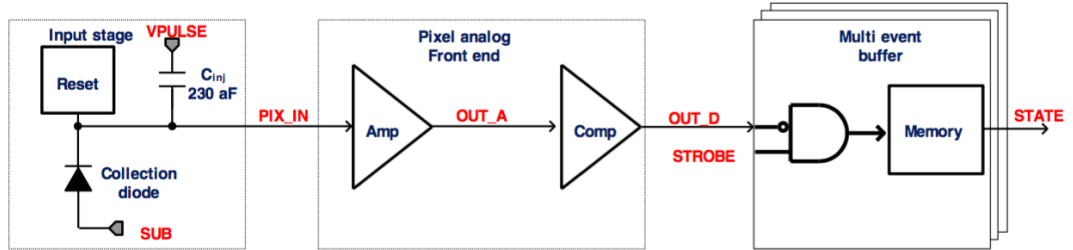


Figure 2.6: Scheme of the in-pixel signal processing, taken from [23].

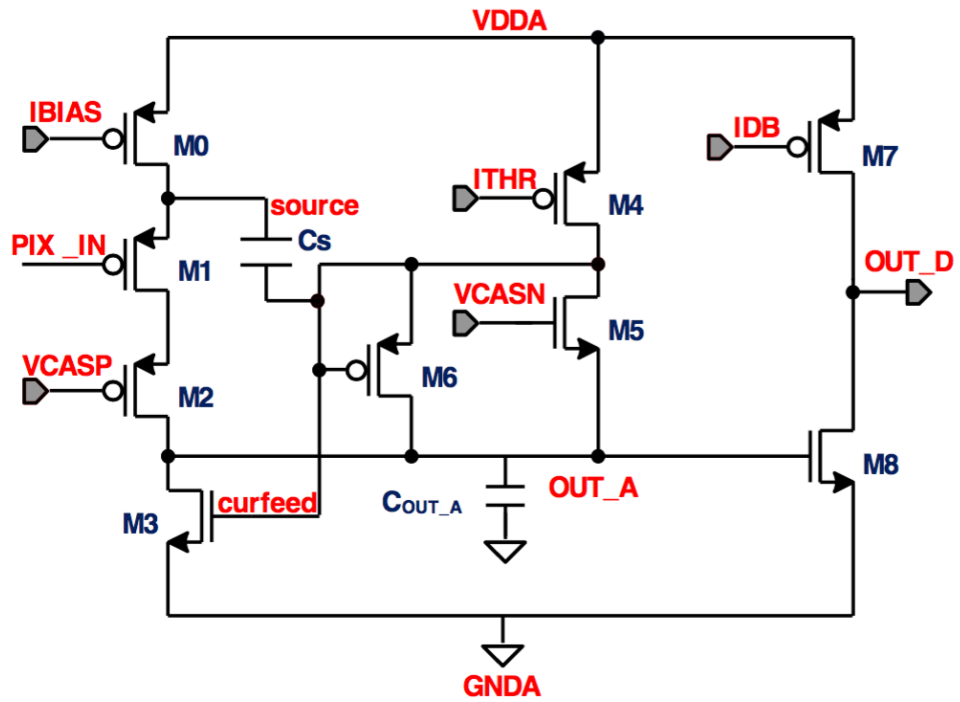


Figure 2.7: Analog front-end schematic practical implementation, taken from [23].

Chapter 3

Experimental Setup for radiation hardness tests of ALPIDE

The main goal of this work is to test the radiation hardness of the ALPIDE chip. In this chapter, we will describe the experimental setup used for radiation hardness tests at the U-120M cyclotron.

3.1 Cyclotron U-120M

A cyclotron is a cyclic accelerator of charged non-relativistic heavy particles, protons and heavy nuclei, with a constant magnetic field [26]. A typical cyclotron scheme is shown in Fig. 3.1. Heavy charged particles are injected from an ion source located at the center. The vacuum chamber is placed in a magnetic field which curves particle trajectories. Acceleration takes place between electrodes (dees), where the electrical field has a constant frequency. Dees have a shape of a hollow cylinder. Original cyclotrons had two dees, however, nowadays they may have more of dees.

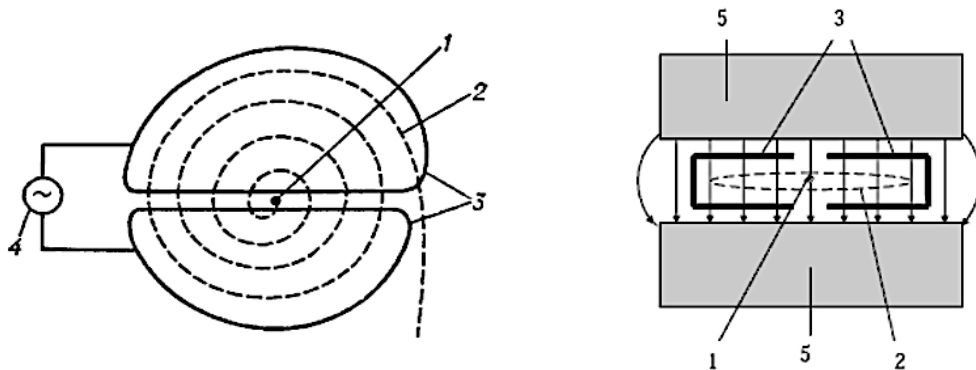


Figure 3.1: Scheme of a simple cyclotron: 1 is an ion source of particles, 2 is a trajectory of accelerated particles, 3 are dees, 4 is a generator of electric field, 5 is an electromagnet, taken from [26].

Considering that the vacuum chamber is placed in a homogeneous magnetic field B , we can calculate a radius of particle trajectory R from the balance of the Lorentz force and centrifugal force.

$$R = \frac{mv}{QB}, \quad (3.1)$$

where v is velocity, m is particle mass and Q is its electric charge. The orbital frequency f of a beam particle is then

$$f = \frac{v}{2\pi R} = \frac{QB}{2\pi m}. \quad (3.2)$$

The acceleration of a particle between dees leads to increase of its kinetic energy E and the radius of the trajectory R . The kinetic energy of a particle at given radius can be calculated as

$$E = \frac{mv^2}{2} = \frac{Q^2 B^2 R^2}{2m}, \quad (3.3)$$

from where the velocity v is

$$v = \frac{QBR}{m}.$$

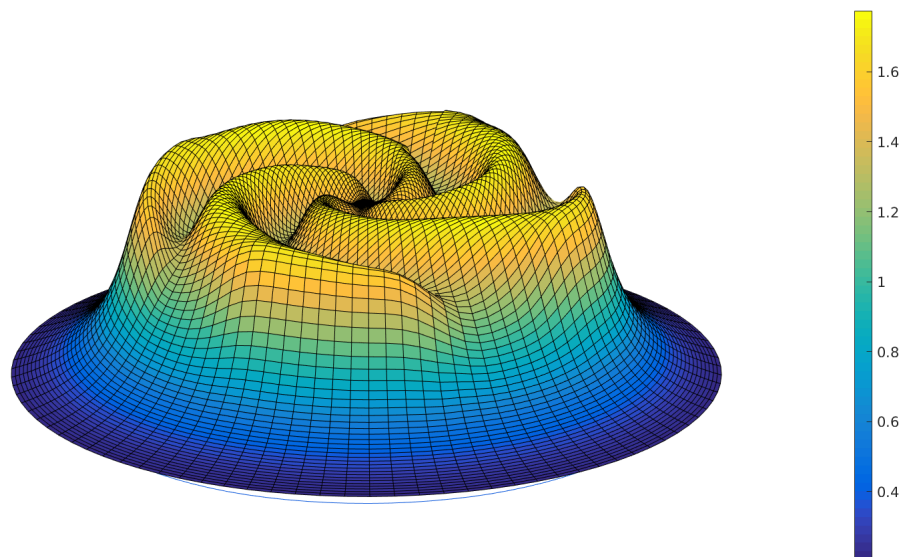


Figure 3.2: Distribution of magnetic field in the U-120M cyclotron in the horizontal plane going through the center of the vacuum chamber. The z axis shows the intensity of the field in Tesla, taken from [27].

Only the particles that pass between dees in a narrow time interval when the voltage between them is the highest fulfill the condition for subsequent acceleration. The probability of successful particle acceleration decreases with an increasing phase difference.

The homogeneous magnetic field, however, does not guarantee the focusing of the beam in cyclotron [28]. Therefore modern cyclotrons use a magnetic field that changes with azimuth [28]. For instance, in Fig. 3.2, we illustrate the configuration of the magnetic field in the U-120M cyclotron [27]. Such field modulation can also compensate for the relativistic increase of particles' mass, therefore ensuring the condition of isochronism [29].

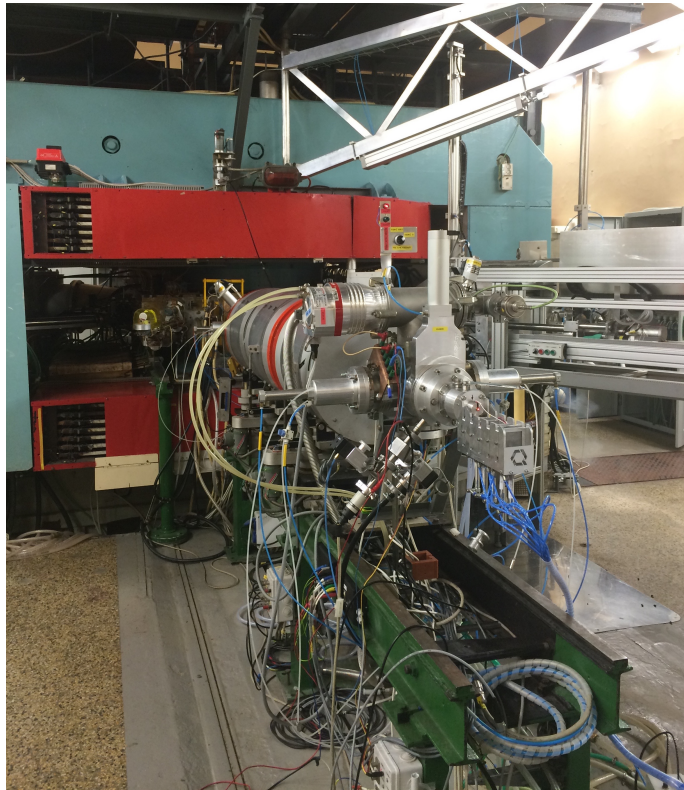


Figure 3.3: Cyclotron U-120M in the Nuclear Physics Institute of the Czech Academy of Sciences in Řež. The beamline for protons and deuterons, extracted in the negative regime, is terminated by the energy degrader unit.

To irradiate the ALPIDE chips, we used the isochronous cyclotron U-120M, which is located in the Nuclear Physics Institute of the Czech Academy of Sciences in Řež [30], see Fig. 3.3. This cyclotron has only one dee electrode, the function of the second dee takes the grounded vacuum chamber wall. The cyclotron is able to accelerate positive ions H^+ , D^+ , ${}^3He^{+2}$ and α and negative ions H^- , D^- . In Tab. 3.1 the parameters of the beam, that can be provided by the cyclotron, are shown. Positive and negative particles are accelerated in two different modes. Each mode has a different extraction

mechanism. The positive mode is used for the acceleration of positive ions. It uses a magnetic kicker in combination with a system of electrostatic deflectors, see Fig 3.4 left. The negative mode accelerates negative ions, the polarity of the extrinsic magnetic field is reversed in this mode, so particles are accelerated in the same direction as in the positive mode. When passing through a 1 μm thick carbon foil, negative ions lose valence electrons and become positive. The final positively charged beam is then bent out of the vacuum chamber by the Lorentz force and is directed to a short beamline, see Fig 3.4 right. The beamline is equipped with 3 quadrupole magnets, which focus the beam and it is terminated with a 55 μm thick aluminum exit window. When compared to the positive mode, the negative mode has higher efficiency of beam extraction, because the positive mode has large beam losses on the electrostatic deflectors. On the other hand, the negative regime has greater uncertainty in the extracted energy of the final beam (about 0.25 MeV [31]). In our tests, the negative mode was used.

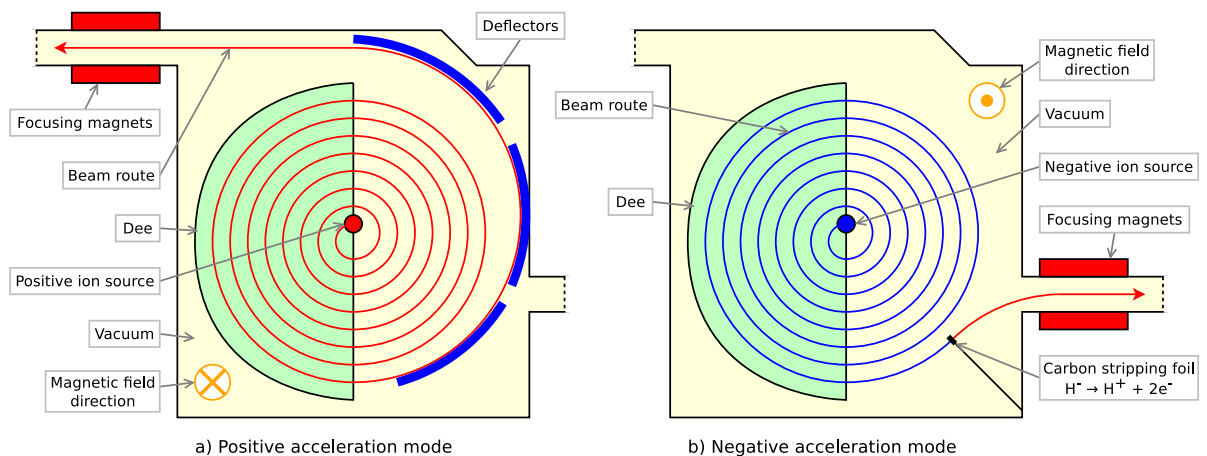


Figure 3.4: Acceleration modes of the cyclotron U-120M, taken from [32].

Ion	E [MeV]	I_{\max} [μA]
H^+	6–25	5
H^-	6–37	50–30
D^+	12–20	5
D^-	11–20	35–20
${}^3\text{He}^{+2}$	18–52	2
α	24–38	5

Table 3.1: Kinetic energies and currents of accelerated particles in the cyclotron U-120M that can be achieved, taken from [29].

The time structure of the beam is shown in Fig. 3.5. The cyclotron works in the radio-frequency (RF) region 10–25 MHz [29]. The RF system is not

operated in a continuous wave regime [31]. The RF acceleration system is protected against discharges by modulating the RF frequency with a 150 MHz signal. This corresponds to a duty cycle period of 6.67 ms. The maximum allowed duty cycle (filling) can be changed in a range 4–65% of the period, it depends on the generator frequency and on the number of particles in the acceleration chamber. The maximally allowed duty cycle for 35 MeV is 20%. In ALPIDE beam tests, we operate with lower duty cycles (5%) to reduce the proton beam intensity.

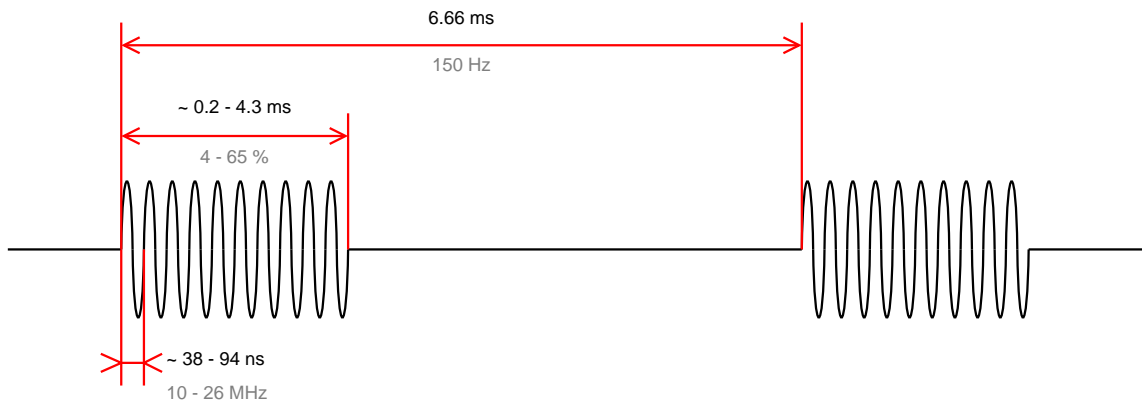


Figure 3.5: Time structure of the acceleration RF electrical field in the U-120M cyclotron. Filling can be varied between 4–65%, this corresponds to 0.2 – 4.3 ms long cycles when the cyclotron accelerates particles. This time is divided by RF to 38–94 ns long RF buckets, taken from [32].

3.2 Ionization chamber PTW 30010 Freiburg

The proton flux from the cyclotron is measured by an ionization chamber. In our measurement, the ionization chamber PTW 30010 Freiburg was used [33]. This chamber has a coaxial cylindrical geometry of an aluminum anode and a graphitic cathode. The surface of the cathode has a protective layer of Polymethylmethacrylate (PMMA). The chamber is filled with air which has atmospheric pressure. The average energy needed for electron-ion pair creation is thus 34 eV [34]. The sensitive volume of this chamber is 0.6 cm³. The nominal working voltage is 400 V. The time of charge collection is 0.14 ms [33]. The ionization chamber PTW 30010 Freiburg and its scheme are shown in Fig. 3.6. Ionization current from the chamber is measured by the microprocessor-controlled universal dosimeter PTW - UNIDOS E [35], which is used also to set the working voltage in the chamber.

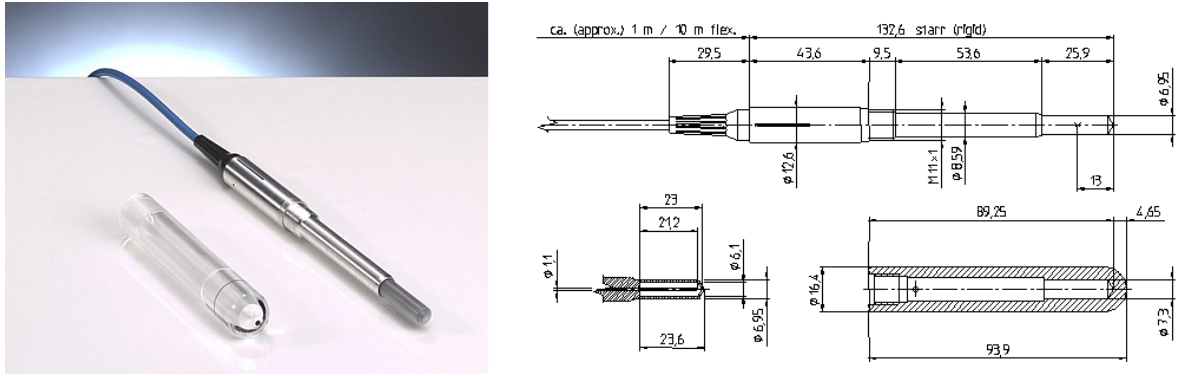


Figure 3.6: Left: Photo of the ionization chamber PTW 30010 Freiburg, taken from [33], Right: The layout of the ionization chamber PTW 30010 Freiburg. All dimensions are in millimetres. Thickness of the PMMA layer and the graphitic cathode is 0.335 mm and 0.09 mm, respectively. The diameter of the aluminum anode is 1.1 mm, taken from [33].

3.3 Setup for irradiation tests at the U-120M cyclotron

The experimental setup for irradiation is shown in Fig 3.7. The beamline is terminated with a pneumatically controlled energy degrader unit, see Fig 3.8. This unit allows either to stop the beam or to change the beam profile and energy by insertion of aluminum plates of different thicknesses into the beam. The first plate is 8 mm thick and serves as a beam stop. The second plate is 0.55 mm thick and it is used during ALPIDE irradiations to make the beam profile wider.

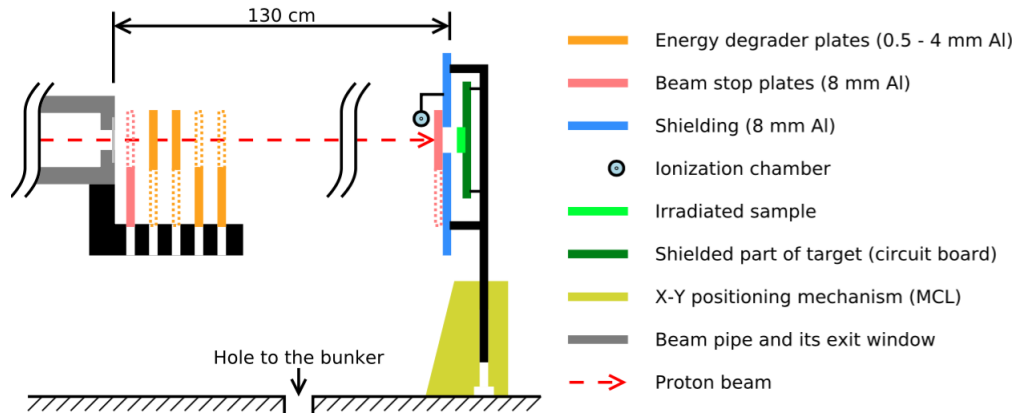


Figure 3.7: Illustration of the beam route from the beamline exit window to the irradiated sample through the energy degrader unit. The sample, the beam stop plate and the ionization chamber are mounted on a remotely controlled stage that allows moving the setup in the plane perpendicular to the beam.



Figure 3.8: Photo of the degrader unit with aluminum plates behind the beamline exit window. During the irradiation, we used the 0.55 mm thick aluminum plate to make the beam profile wider. The initial energy of the proton beam is about 35 MeV. After passing through the degrader plate and air it reduces to ~ 30 MeV at the sample position.

The irradiated sample (ALPIDE) is placed 130 cm away from the beamline exit window at a remotely movable stage together with the ionization chamber and an additional beam stop plate, see Fig 3.9 and Fig 3.10. The

movable stage can move the setup independently along the x and y axes with a step of 1 mm. The movable stage is controlled from a PC placed in the cyclotron control room, see Fig 3.10.

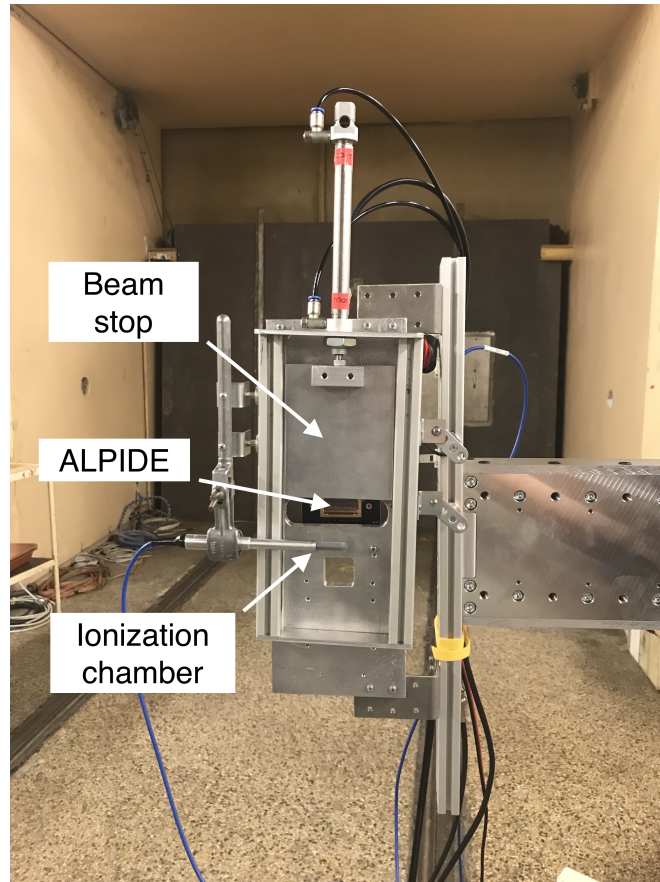


Figure 3.9: Photo of the frame with the ionization chamber, beam stop plate and the ALPIDE chip, all placed on an arm of the movable stage. The relative position of ALPIDE and the ionization chamber is fixed, the beam stop plate covers the chip during the beam profile scanning.

The relative position of an irradiated sample and the ionization chamber on the setup is fixed and is measured with the precision of 1 mm before each irradiation using a laser tracker. The laser beam from the tracker shows an approximate position of the beam spot at the setup. Then we navigate the movable stage to the position in which the ionization chamber is in the laser spot and we pencil the corresponding coordinates. After that, the stage is moved such that the center of the ALPIDE chip gets to the laser spot. The relative position of the ALPIDE and the ionization chamber is given by the difference between these two positions. The ionization chamber is used for on-line flux monitoring during the irradiation and for beam transverse profile scanning before the sample irradiation. The beam stop plate between the ionization chamber and the sample serves to prevent the sample from being irradiated during the beam profile scanning.

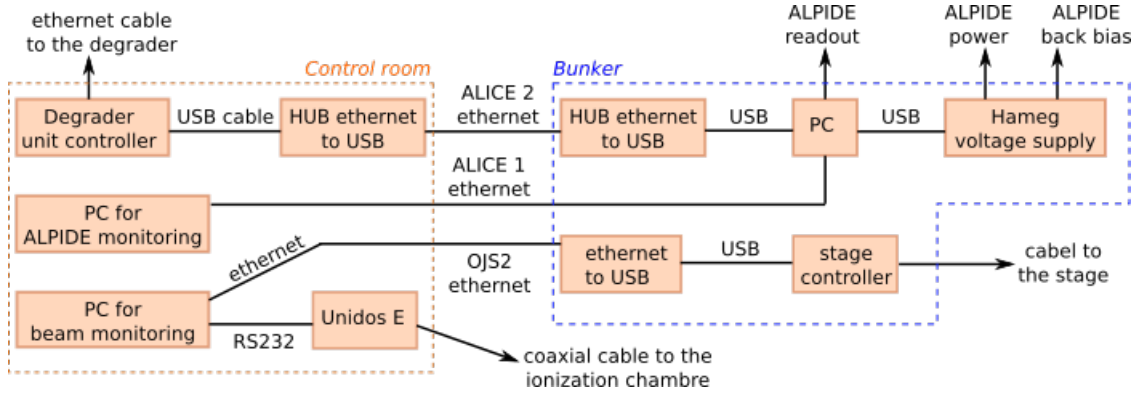


Figure 3.10: The logical connection of all basic devices for sample positioning and proton flux measurement used during the irradiation tests. The electronics for ALPIDE operation and stage controller is placed in the bunker under the cyclotron hall. The ethernet cables are used to transfer signals over the long distance (≈ 40 m) between the control room and the bunker.

The scheme of cable network between all devices used in the test is shown in Fig 3.10. The PC operating the ALPIDE chip, the energy degrader unit and the voltage source for ALPIDE is placed in the bunker below the cyclotron hall. For its operating, the PC in the control room is used. Another PC is used for beam monitoring and movable stage operation.

3.4 The irradiation process

The experiment at the cyclotron is made in the following way. First, the position calibration of the movable stage is done. Then the ALPIDE is shielded with the second beam stop mounted on the movable stage and the beam profile along the horizontal and vertical axes is measured. The profiles are scanned stepwise in the traverse plane to the beam by moving the entire setup which is mounted at the end of the stage arm, see Fig. 3.9. The scan of the ionization chamber current takes about 1 minute for each axis.

After each scan, the measured beam profiles are parametrized by a 1-dimensional Gaussian function, which gives the coordinates of the beam center with respect to the stage and the widths of the beam along the horizontal and vertical axes, see Fig 3.11.

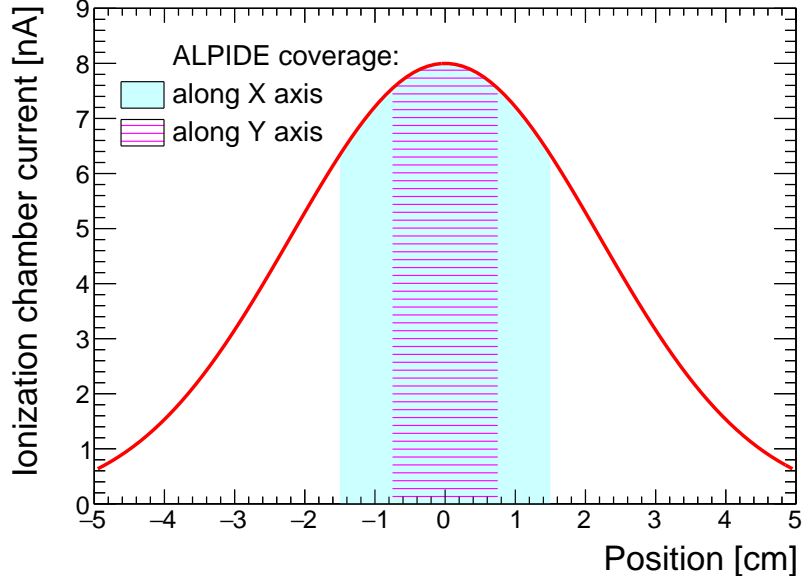


Figure 3.11: Beam profile measured by the ionization chamber in the case when the beam passed through the 0.55 mm thick aluminum plate (red line). The width of the beam is about 2 cm (standard deviation). The light blue and the hatched region correspond to ALPIDE coverage in horizontal and vertical directions.

From the fit, we can determine the coordinates of the center of the beam with an accuracy of 1 mm and the transverse width of the beam. Knowing the relative vertical distance between the center of ALPIDE and the center of the ionization chamber, we can determine the coordinates of the ALPIDE center.

In the next step, the second beam stop still covers the ALPIDE chip and the ionization chamber is placed at the beam center and the intensity of the beam is measured and tuned. After moving the stage to the position when the ALPIDE would be in the beam center, the current in the ionization chamber declines and is corrected by a factor determined from the known Gaussian beam profile. During the irradiation, we monitor ionization chamber current and use it to calculate instantaneous proton flux P with 10% accuracy [36, 37, 31]:

$$P = I \cdot k, \quad (3.4)$$

where I is a current measured by the ionization chamber and k is a known calibration parameter [36, 37]. Proton fluence F can be calculated by integrating the flux P :

$$F = \int_{t_0}^{t_0+t_{\text{irr}}} P dt, \quad (3.5)$$

where t_0 is a time of the beginning of the irradiation and t_{irr} is a period of the irradiation. Finally, the total ionizing dose D is estimated by the formula [38]:

$$D[\text{krad}] = 1.602 \times 10^{-8} \times \text{LET}[\text{MeV} \cdot \text{cm}^2 \cdot \text{mg}^{-1}] \times F[\text{cm}^{-2}], \quad (3.6)$$

where LET is the stopping power of 30 MeV protons in a given material (in our case in silicon). The formula is derived in Appendix A. The value of LET is taken from Stopping and Range of Ions in Matter (SRIM) simulation [39], the dependence of LET in silicon on the energy of protons is shown in Fig. 3.12. The non-ionizing energy loss induced by the 30 MeV proton beam is then calculated as follows [40]:

$$\text{NIEL} [1 \text{ MeV n}_{\text{eq}} \text{ cm}^{-2}] = 2.346 \times F [\text{cm}^{-2}]. \quad (3.7)$$

The coefficient 2.346 is a tabled value taken from [41].

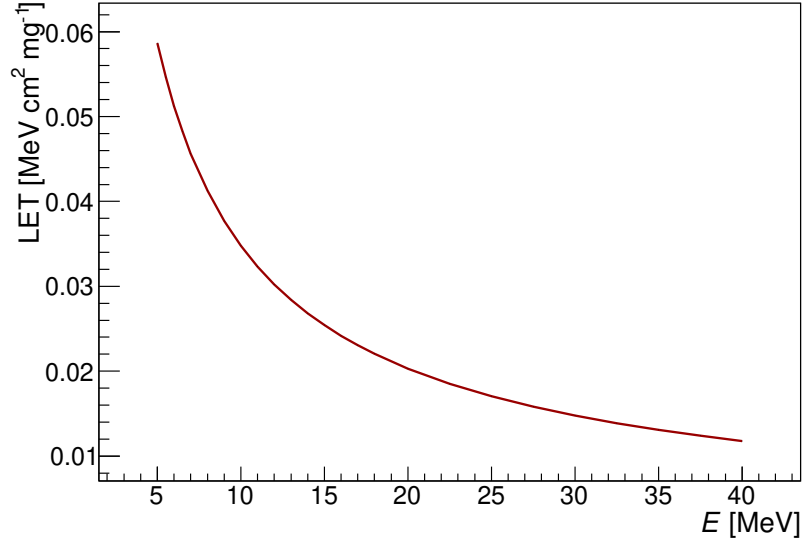


Figure 3.12: Stopping power of protons versus proton energy, data from [39].

	Default settings	Settings from 11.2017
V_{CASN}	105	90
V_{CASN2}	117	102
V_{RESETP}	117	117
V_{RESETD}	147	147
V_{CLIP}	60	60
I_{THR}	51	51
I_{DB}	64	64
I_{RESET}	100	100

Table 3.2: Default DAC parameters and the parameters set from November 2017. Values of the parameters are given in DAC units.

It is important to note that the irradiation of the chip is not continuous. The irradiations are interrupted by measurement of the sensor activation

function (the so-called threshold scan) and the DAC scan. The goal of the DAC scan is to test the response of the voltage and current sources which are implemented on the chip. While performing these scans the ionization chamber and the tested ALPIDE chip are covered by the first beam stop plate and are not irradiated. Then the chip is uncovered again and analog and digital currents are monitored. After that, the whole cycle is repeated. The measurement stops when the value of the analog current reaches half of the initial value. This prevents that the chip gets destroyed. The default DAC settings are shown in Tab.3.2. Since November 2017, V_{CASN} was set to a lower value (90) and V_{CASN2} was set to 102 to increase the threshold. During the irradiation, the sensors are supplied with a voltage of 5 V and a moderate substrate reverse bias of -3 V. Due to the fact that the chips are sensitive to the light, all measurements are made in darkness. The irradiation hardness tests are performed at room temperature.

Chapter 4

Analysis of radiation hardness tests at the U-120M cyclotron

In real conditions at the LHC, the ALPIDE sensors placed in the innermost layer of the ITS IB will get the integrated total ionization dose of 270 krad (integral over the Run 3 and Run 4). The expected average dose rate will be however very small and it is supposed that annealing of radiation damage will have a positive influence on the detector functionality. The detector proposal expects that the chip should nevertheless survive an integrated dose that is ten times higher [8]. To reach 2700 krad with the same dose rate as expected at the LHC would take several years of irradiation. This, however, cannot be done at the U-120M cyclotron due to economical and time reasons. Therefore the aim was to get reasonably close to the real conditions at the LHC and to divide the accumulated dose to a longer time period.

Radiation hardness of ALPIDE was tested in a series of measurements made at the cyclotron U-120M since September 2016. Chips are irradiated by a flux of 30 MeV protons and typically obtain a dose of 100 krad during one session. After the irradiation, the chips are left at rest at the room temperature to anneal and their state is monitored.

The radiation hardness tests were made for two chips: A4W7G7R38 and A4W7G7R41. Those chips present the final design of ALPIDE. The thickness of the epitaxial layer is 25 μm .

I analyzed log files from the irradiations and in Tab. 4.1 and Tab. 4.2 I present total ionizing doses, proton fluence and NIEL accumulated during the irradiations from September 2016 to July 2018, dose rates and average fluxes. Those parameters were obtained based on the current measured by the ionization chamber. Total ionization dose and proton fluence achieved during different irradiation campaigns are shown in Fig. 4.1 and 4.2. As can be seen, the dependences are gradational. In the periods, where the dependence is flat, the beam was blocked and the measurements of the DAC characteristics and the activation function (threshold scan) were made. From Fig. 4.1, 4.2 it is seen that the chip A4W7G7R38 was irradiated

initially much faster than the chip A4W7G7R41. This was done in order to study whether the radiation damage depends also on the ionization dose rate. In the first irradiation, the average dose rate for A4W7G7R38 was about $60 \text{ rad}\cdot\text{s}^{-1}$ while for A4W7G7R41 it was about $18 \text{ rad}\cdot\text{s}^{-1}$. Let us point out, that the required 2.7 Mrad was achieved by the chip A4W7G7R41 only on July 2018 and by the chip A4W7G7R38 in May 2019. Comparing the values of accumulated doses for both chips in Tab. 4.1 and Tab.4.2 it is seen that on average the chip A4W7G7R38 obtained lower radiation load than the chip A4W7G7R41. This difference in radiation hardness is assumed to be a consequence of the difference in dose rate during the first irradiation.

Date	D [krad]	TID [krad]	F [10^{10} cm^{-2}]	F_{tot} [10^{10} cm^{-2}]	D rate [$\text{rad}\cdot\text{s}^{-1}$]	\bar{P} [$10^8 \text{ cm}^{-2}\cdot\text{s}^{-1}$]	NIEL [$10^{10} \text{ 1 MeV}_{\text{neq}} \text{ cm}^{-2}$]
9.2016	341	341	145	145	59.9	2.6	340
10.2016	122	463	52	197	64.7	2.8	462
12.2016	122	585	52	249	38.6	1.6	583
1.2017	89	675	38	287	49.1	2.1	672
3.2017	78	752	33	320	37.9	1.6	750
4.2017	90	842	39	358	18.8	0.8	840
5.2017	86	929	37	395	17.5	0.7	926
6.2017	96	1024	41	435	40.9	1.7	1021
7.2017	87	1111	37	472	34.2	1.5	1107
8.2017	94	1204	40	512	32.9	1.4	1201
9.2017	86	1290	36	548	32.9	1.4	1286
10.2017	87	1377	37	585	24.6	1.1	1373
11.2017	84	1461	36	621	30.7	1.3	1457
1.2018	108	1569	46	667	31.8	1.4	1564
2.2018	111	1680	47	714	34.9	1.5	1675
3.2018	110	1791	47	761	32.6	1.4	1785
4.2018	95	1886	40	801	31.5	1.4	1880
5.2018	114	2000	49	850	38.8	1.7	1994
6.2018	100	2100	43	893	36.3	1.6	2094
7.2018	24	2124	10	903	22.3	1.0	2227
10.2018	156	2390	66	1016	37.0	1.6	2383
1.2019	136	2526	58	1073	33.2	1.4	2518
5.2019	174	2700	734	1147	31.4	1.4	2692

Table 4.1: Summary of the irradiation campaigns of the chip A4W7G7R38, where D is dose, TID is accumulated ionization dose, F is fluence, F_{tot} is total fluence, P is a proton flux, \bar{P} is an average proton flux and NIEL is accumulated non-ionizing energy loss.

Date	D [krad]	TID [krad]	F [10^{10} cm^{-2}]	F_{tot} [10^{10} cm^{-2}]	D rate [rad·s $^{-1}$]	\bar{P} [$10^8 \text{ cm}^{-2}\cdot\text{s}^{-1}$]	NIEL [$10^{10} \text{ 1 MeV}_{\text{neq}} \text{ cm}^{-2}$]
9.2016	338	338	144	144	17.8	0.8	337
10.2016	171	509	73	217	65.3	2.8	508
12.2016	140	649	60	276	72.1	3.1	647
1.2017	125	774	53	329	30.9	1.3	771
3.2017	113	886	48	377	37.5	1.6	884
4.2017	94	980	40	416	27.4	1.2	977
5.2017	100	1080	43	459	34.8	1.5	1077
6.2017	115	1195	49	508	36.5	1.6	1192
7.2017	116	1311	49	557	24.2	1.0	1307
8.2017	118	1429	50	607	36.2	1.5	1425
9.2017	122	1551	52	659	37.0	1.6	1546
10.2017	112	1663	48	707	33.8	1.4	1658
11.2017	120	1782	51	758	29.4	1.3	1777
1.2018	130	1912	55	813	31.9	1.4	1906
2.2018	115	2027	49	861	42.3	1.9	2021
3.2018	138	2165	59	920	40.7	1.8	2159
4.2018	155	2320	66	986	36.1	1.6	2313
5.2018	142	2461	60	1046	34.7	1.5	2454
6.2018	160	2621	68	1114	39.0	1.7	2614
7.2018	79	2700	34	1148	24.6	1.1	2692
10.2018	121	2821	52	1199	56.1	2.4	2813

Table 4.2: Summary of the irradiation campaigns of the chip A4W7G7R41, where D is dose, TID is accumulated ionization dose, F is fluence, F_{tot} is total fluence, P is a proton flux, \bar{P} is an average proton flux and NIEL is accumulated non-ionizing energy loss.

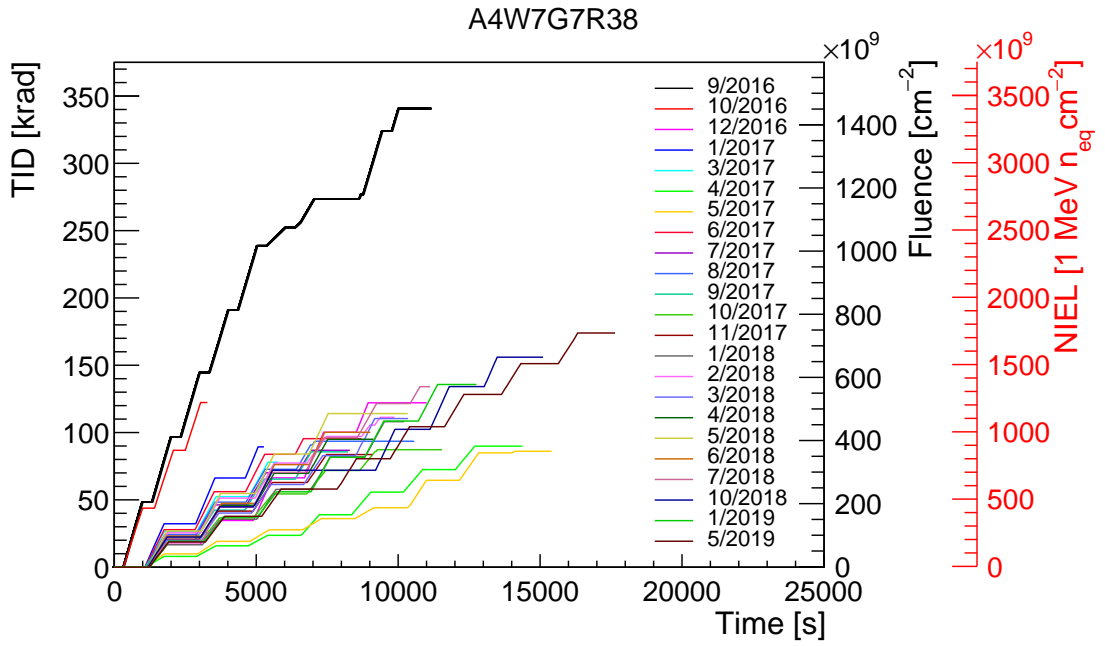


Figure 4.1: Total ionization dose and accumulated proton fluence and NIEL for different irradiation campaigns of the chip A4W7G7R38.

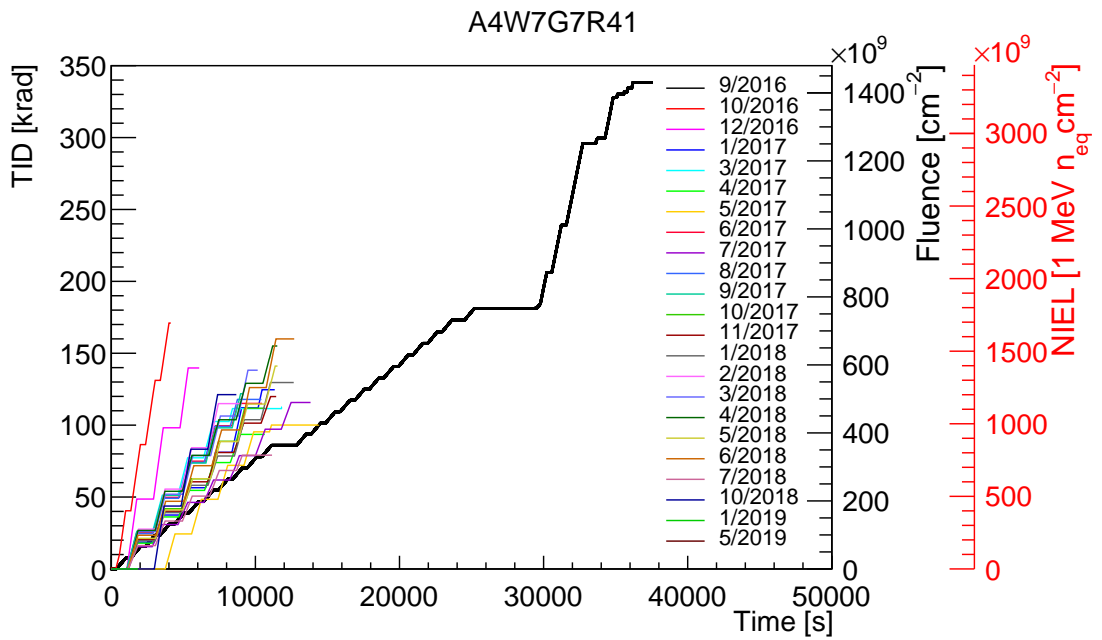


Figure 4.2: Total ionization dose and accumulated proton fluence and NIEL for different irradiation campaigns of the chip A4W7G7R41.

4.1 Estimate of NIEL induced by secondary neutrons

Since the proton beam from the cyclotron interacts with the aluminum plates in the energy degrader and with the air, a field of secondary neutrons is created. These neutrons can also hit the chip and induce NIEL. In this section, I describe a Geant4 [43] simulation I used to assess, how intensive the flux of the secondary neutrons is and I give an estimate of the associated NIEL.

Geant4 is a Monte Carlo based simulation tool to calculate particle production and transport through material. Geant4 was developed in CERN and it is based on C++.

Basic objects used in my Geant4 analysis were the following ones:

- MyDetectorConstruction.cc: defines the geometry of setup,
- MyDetectorMessenger.cc: decodes the configuration files and sets the parameters of beam protons and the setup,
- MyRunAction.cc: is called once per run and it is used to declare output histograms,
- MyPrimaryGeneratorAction.cc: defines the momentum and the emission point of the proton beam particle,
- MyEventAction.cc: defines the analysis steps that are done every event,
- MySteppingAction.cc: finds a particle in a certain volume, checks that it was a neutron and stores the energy it carries.

There are 4 different configurations of the experimental setup that are often used in our tests that I simulated:

- The first configuration corresponds to the setup which is used during the chip irradiation. In this case, only one 0.55 mm thick aluminum plate is inserted in the proton beam, see Fig. 4.3 a).
- The second configuration is used while making the DAC and the threshold scans. It contains the first beam stop plate in the energy degrader unit and the 0.55 mm thick aluminum plate, see Fig. 4.3 b).
- In the third configuration, the 0.55 mm thick aluminum plate and two beam stop plates are used (the first beam stop plate is in the energy degrader unit and the second one is in front of the ALPIDE), see Fig. 4.3 c). This configuration is sometimes used when the cyclotron operators tune parameters of the proton beam.
- The fourth configuration includes the 0.55 mm thick aluminum plate and the beam stop plate in front of the ALPIDE, see Fig. 4.3 d). This setup was used during the beam profile scan made by the ionization chamber.



a) Configuration 1



b) Configuration 2



c) Configuration 3



d) Configuration 4

Figure 4.3: Sketches of all four configurations of the experimental setup from the Geant4 simulation. From the left to the right: a) beamline exit window, 0.55 mm thick aluminum energy degrader plate, ALPIDE; b) beamline exit window, 8 mm thick aluminum beam stop plate, 0.55 mm thick aluminum energy degrader plate, ALPIDE; c) beamline exit window, 8 mm thick aluminum beam stop plate, 0.55 mm thick aluminum energy degrader plate, the second 8 mm thick aluminum beam stop plate and the ALPIDE; d) beamline exit window, 0.55 mm thick aluminum energy degrader plate, 8 mm thick aluminum beam stop plate and the ALPIDE. The blue line corresponds to the track of the protons and yellow points show the interaction points.

All 4 setup configurations were simulated using the QBBC physics list [43]. Beam protons had a kinetic energy of 34.97 MeV and were fired along the z axis. The simulated setup included also the 55 μm thick aluminum beam pipe exit window, which is in front of the energy degrader unit. The ALPIDE was located 130 cm from the beam pipe exit window along the beam direction. The whole mother volume was filled with air. The number of beam protons simulated for each configuration was about 3×10^9 . The energy of neutrons was measured in a 1 μm thick vacuum gap right in front of the ALPIDE. This was done using the MySteppingAction object which was checking if the actual particle in the vacuum gap volume is a neutron (`particle->GetDefinition() == G4Neutron::Definition()`, where `particle` is the `G4Track` object). After detecting the neutron, its energy was filled to a histogram.

For each configuration, I obtained the energy distribution of the neutrons right in front of the ALPIDE. Fig. 4.4 shows the neutron energy distributions normalized per 1 proton, 1 cm^2 and the bin width. The neutrons are created in nuclear reactions, which in general have a small cross section, therefore one proton produces only a small number of secondary neutrons. The mean energy of the generated neutrons is in the range of 3–7 MeV and depends on the chosen configuration.

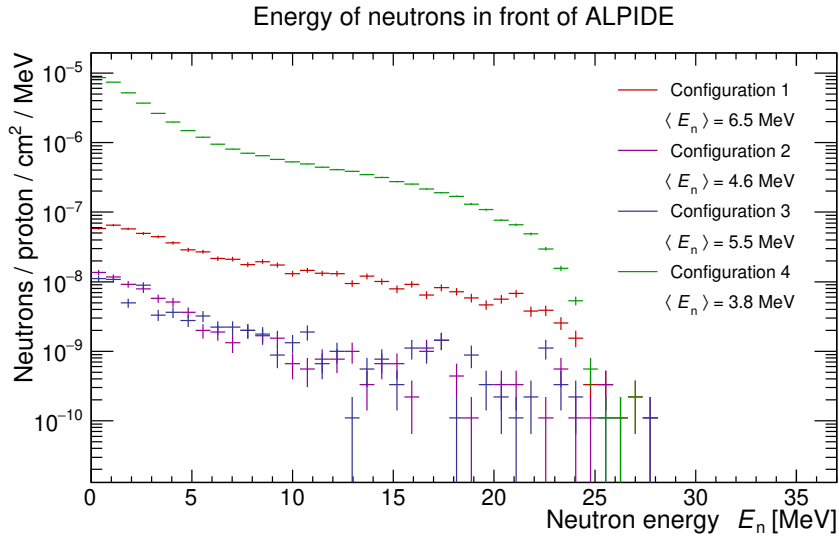


Figure 4.4: The energy spectrum of neutrons in front of the ALPIDE for different configurations of the experimental setup normalized per 1 proton, 1 cm^2 and bin width. The geometries of the configurations are described in the text.

The most intensive neutron field was created in the fourth configuration with the half-millimeter aluminum plate and the second beam stop plate in front of the chip. Since this beam stop plate is close to the chip, the created neutron field is not able to spread enough. In the other configurations, the neutrons are mostly created far away from the ALPIDE.

From the irradiation log files, I have identified the periods: 1) when the chip was irradiated, 2) when the threshold scan and DAC scans took place and

3) when the beam profile was measured. These periods were determined according to the current in the ionization chamber, see Fig. 4.5. For each case, I convoluted the corresponding spectrum of neutrons $N(E_n)$ [cm^{-2}] from Fig. 4.4 with the NIEL coefficients $k_{\text{NIEL}}(E_n)$ [41] and rescaled the result by the proton flux P [$\text{cm}^{-2}\text{s}^{-1}$], integrated over time t [s] and the sensor area A (4.5 cm^2):

$$\text{NIEL} = \int_{E_{\min}}^{E_{\max}} A \cdot k_{\text{NIEL}}(E_n) \cdot N(E_n) dE_n \int_{t_{\min}}^{t_{\max}} P dt. \quad (4.1)$$

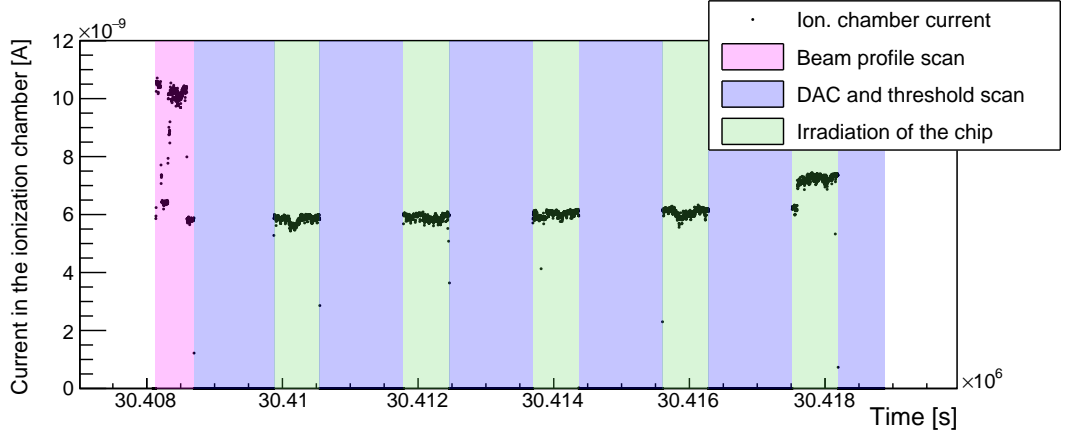


Figure 4.5: Record of the ionization chamber current during the irradiation campaign of the chip A4W7G7R41 on March 2018.

Period of irradiation	NIEL [$1 \text{ MeV n}_{\text{eq}} \text{ cm}^{-2}$]
Irradiation	3.5×10^7
Threshold and DAC scan	6.2×10^6
Beam tuning	4.5×10^8

Table 4.3: Total NIEL contributions from the three configurations used during sensor beam test. The quoted values give the sum over all irradiation campaigns that took place since September 2016.

The total NIEL is the sum of all 3 contributions calculated for every irradiation campaign and presented in Tab. 4.3. During the beam profile measurement, where the whole setup (the ionization chamber, the beam stop plate and the chip) were moving, I assumed, that the chip is in the center of the beam. During the threshold and DAC scan periods, I have assumed that the proton flux did not change w.r.t. the previous irradiation period. Therefore the calculated NIEL is an upper estimate of the real value. Consequently, the total NIEL obtained by the chip A4W7G7R41 from the neutrons is less than $4.9 \times 10^8 \text{ 1 MeV n}_{\text{eq}} \text{ cm}^{-2}$. When this value is compared with the NIEL caused by protons, which is $2.813 \times 10^{13} \text{ 1 MeV n}_{\text{eq}} \text{ cm}^{-2}$ (cf. Tab. 4.2), we can conclude that the secondary neutrons contribute to the

total sensor NIEL negligibly. This simulation, however, does not include the neutron field, which is created by the cyclotron itself. This field was not measured yet and its determination is beyond the scope of this thesis.

4.2 The analysis of threshold and temporal noise

A charge threshold is defined as a charge which is registered by a pixel with a 50 % probability. In ALPIDE sensor charge threshold depends mainly on I_{THR} , which affects the shape of the pulse, and V_{CASN} , which regulates the baseline voltage [19]. With increasing I_{THR} the pulse height and width reduces, which leads to an increase of charge threshold. On the other hand with increasing V_{CASN} the baseline voltage increases and the charge threshold reduces [1].

The measurement of the charge threshold and temporal noise is made by the following method: the same charge Q_{inj} is injected N times by a capacitance C_{inj} in a chosen pixel. After that the activation function $r(Q_{\text{inj}})$ is determined as follows:

$$r(Q_{\text{inj}}) = \frac{N_{\text{hit}}(Q_{\text{inj}})}{N}, \quad (4.2)$$

where $N_{\text{hit}}(Q_{\text{inj}})$ is the number of registered hits and N is the total number of charge injections. Assuming the Gaussian distribution of the temporal noise, the activation function can be parametrized using the Error function as

$$\frac{1}{2} \left[1 + \operatorname{erf} \left(\frac{Q_{\text{inj}} - Q_{\text{THR}}}{\sqrt{2}\sigma} \right) \right], \quad (4.3)$$

where erf is an Error function, which accounts for the smearing of the threshold due to temporal noise, Q_{THR} is the charge needed to activate the pixel with 50% probability and σ is a temporal noise. An example of the experimentally obtained activation function is shown in Fig. 4.6. The curve is sometimes called S-curve.

In Fig. 4.7, I illustrate the evolution of the activation function in one selected pixel with time. Let me point out that since the beginning of irradiations, the threshold was decreasing with the total ionization dose until the beginning of 2018 when the threshold was retuned by lowering V_{CASN} . This is also shown in Fig. 4.7, where we see that in 2018 the activation function moved to the right (the amount of charge needed for pixel activation increased). Nevertheless, the width of the activation region grows throughout all periods (temporal noise grows). In further analysis, I have studied the mean threshold values. The mean threshold values were obtained by averaging over 10% of all pixels. The pixels were chosen such that they were uniformly distributed over the sensor surface. A typical distribution of thresholds obtained from 10% of pixels for both studied sensors is shown in Fig. 4.8. The distributions correspond to the non-irradiated sensors with the default DACs settings.

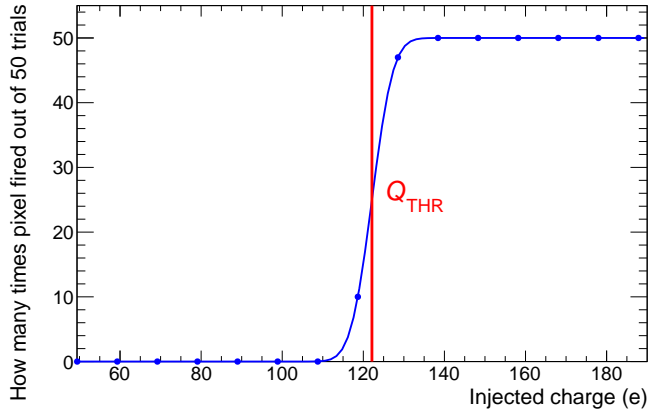


Figure 4.6: Example of an activation function (S-curve) measured for one pixel of the sensor A4W7G7R41 as a function of Q_{inj} .

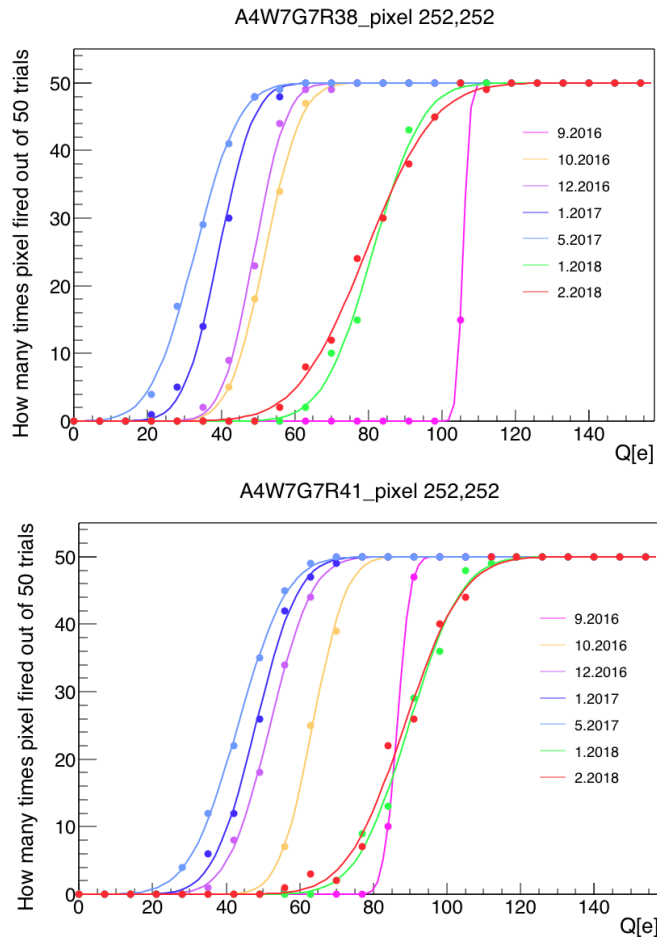


Figure 4.7: S-curve as a function of Q_{inj} measured for the pixel [252, 252] on the chips A4W7G7R38 and A4W7G7R41. Dates of measurements are given in the legend. The curves for other time periods look similarly.

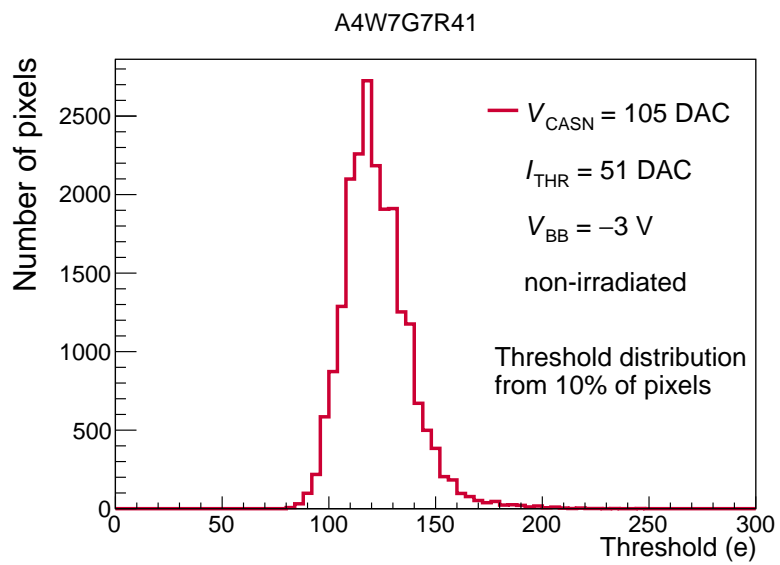
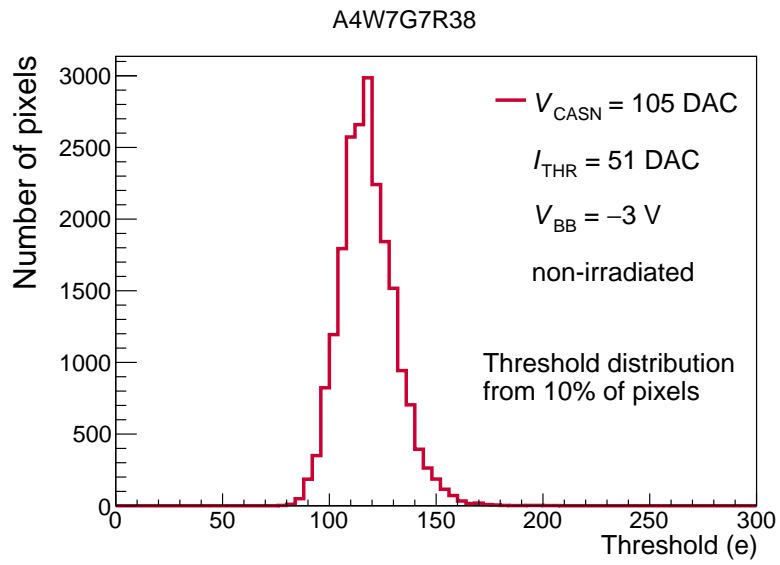


Figure 4.8: The threshold distribution obtained from 10% of pixels for the sensors A4W7G7R38 and A4W7G7R41 with the default DAC settings, see Tab. 3.2.

In Fig. 4.9 and 4.10 I present the dependence of the mean charge threshold on the accumulated dose. As can be seen from the figures, the mean threshold drops with the increasing total ionization dose. However, since November 2017, V_{CASN} settings were changed (see Tab. 3.2) and the mean charge threshold increased. After this change we also observe a visible effect of the annealing on the mean charge threshold (see Chapter 1.4.1). The new settings for V_{CASN} , however, does not lead to a visible decrease in the average temporal noise which keeps rising. The noise keeps decreasing only during the annealing between irradiation campaigns. The dependences of temporal noise on TID for both chips are shown in Fig. 4.11 and 4.12, the annealing process is manifested by a decline of the mean noise. For the threshold tuning in November 2017, it was necessary to investigate how the charge threshold in pixels depends on V_{CASN} settings. This is illustrated in Fig. 4.13 and 4.14. The goal of the tuning was to bring the mean threshold value close to its initial value from September 2016.

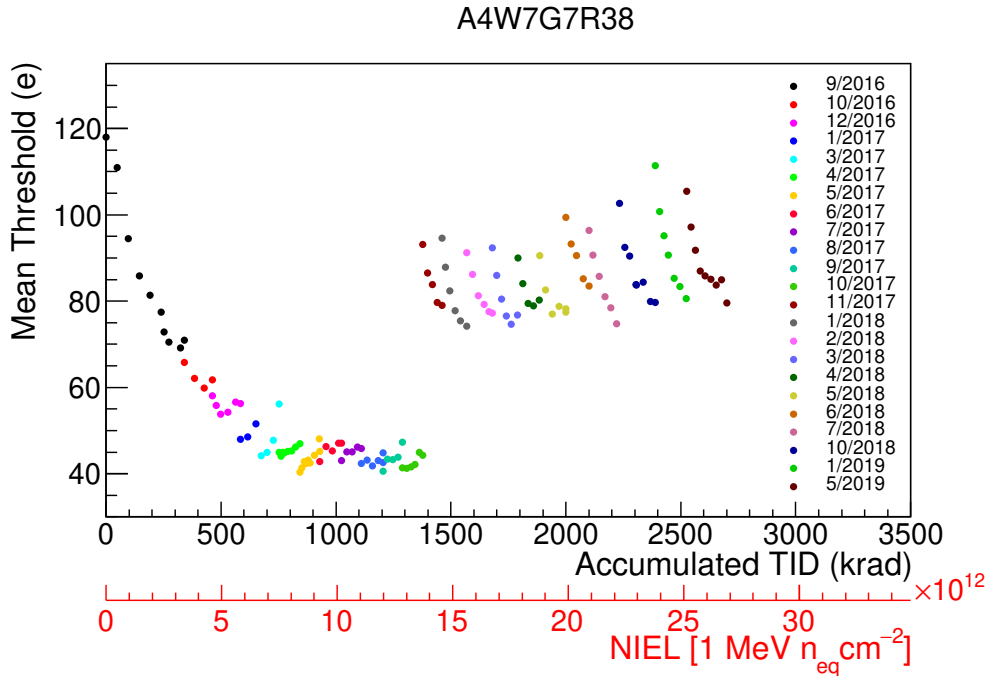


Figure 4.9: Mean threshold vs. accumulated TID and NIEL for the chip A4W7G7R38 for different irradiation campaigns.

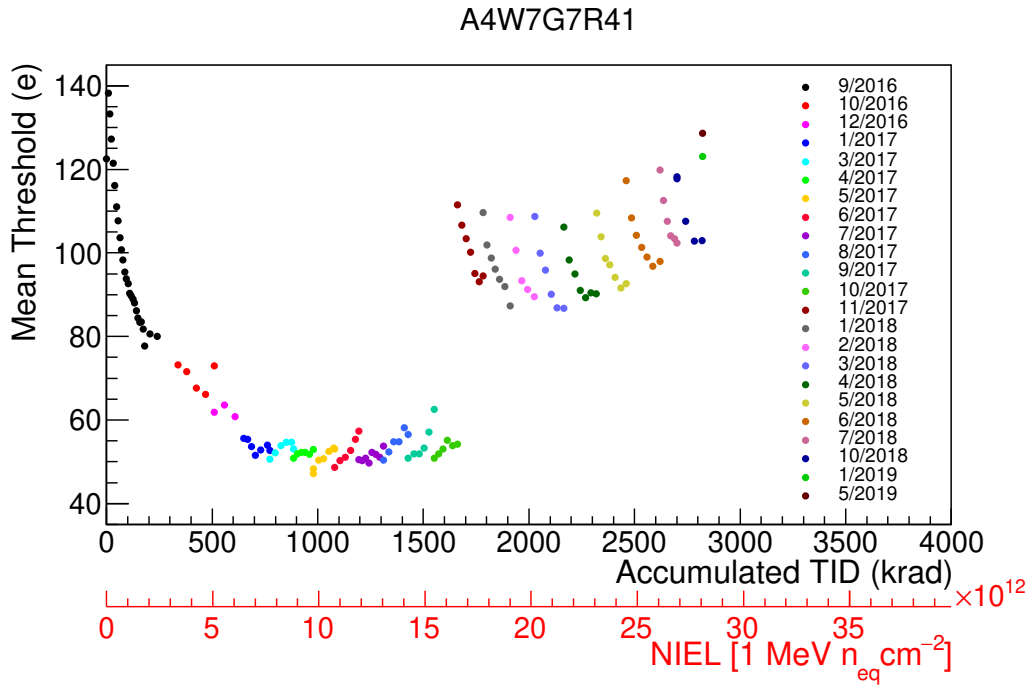


Figure 4.10: Mean threshold vs. accumulated TID and NIEL for the chip A4W7G7R41 for different irradiation campaigns, the last two points correspond to annealing.

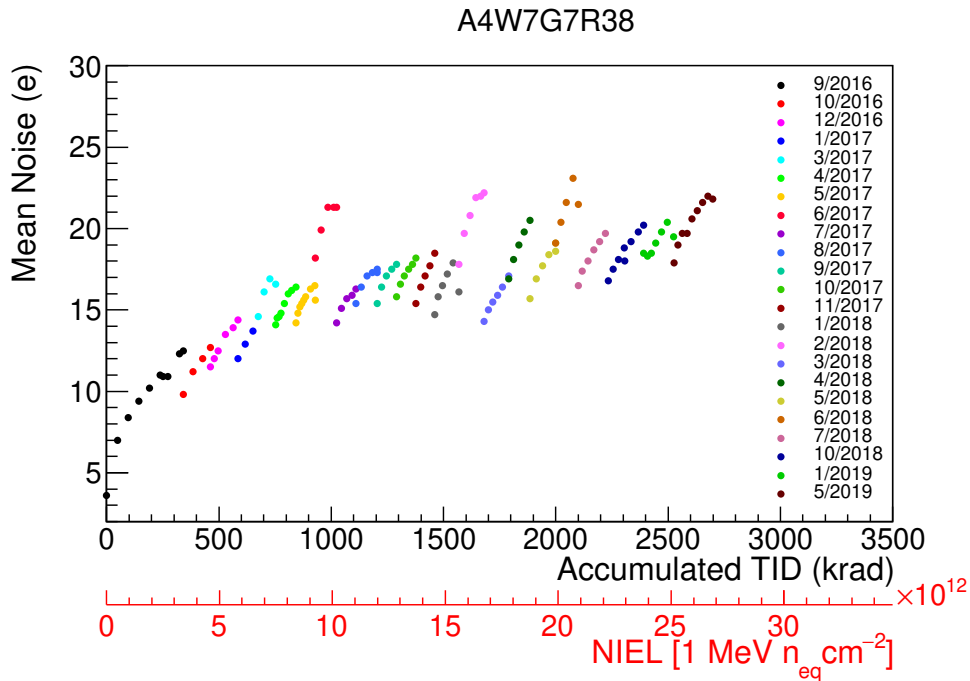


Figure 4.11: Mean noise vs. accumulated TID and NIEL for the chip A4W7G7R38 for different irradiation campaigns.

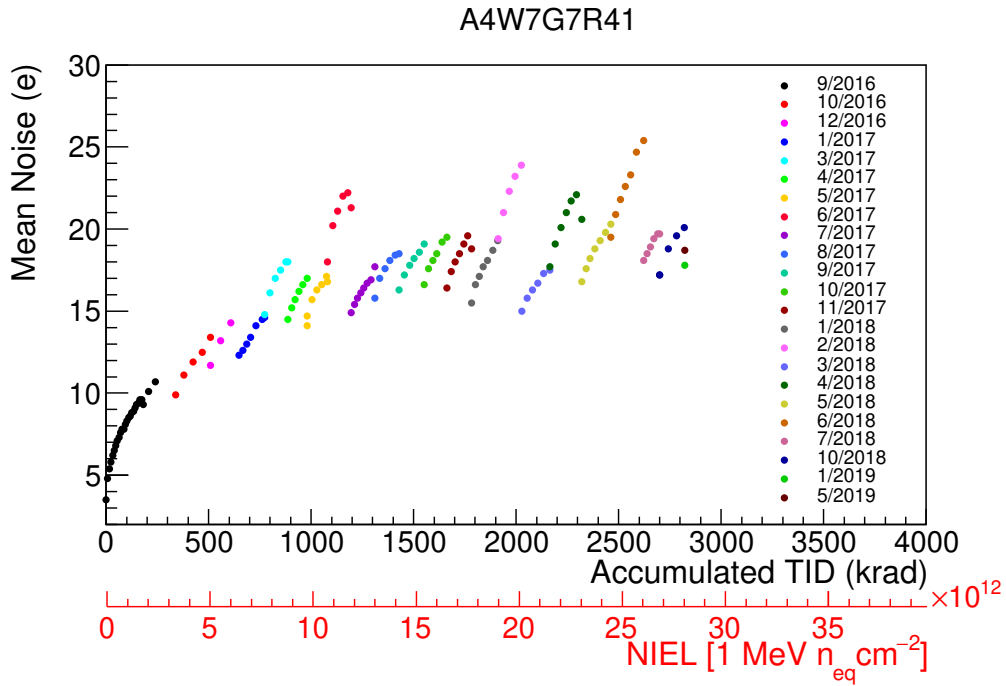


Figure 4.12: Mean noise vs. accumulated TID and NIEL for the chip A4W7G7R41 for different irradiation campaigns, the last two points correspond to annealing.

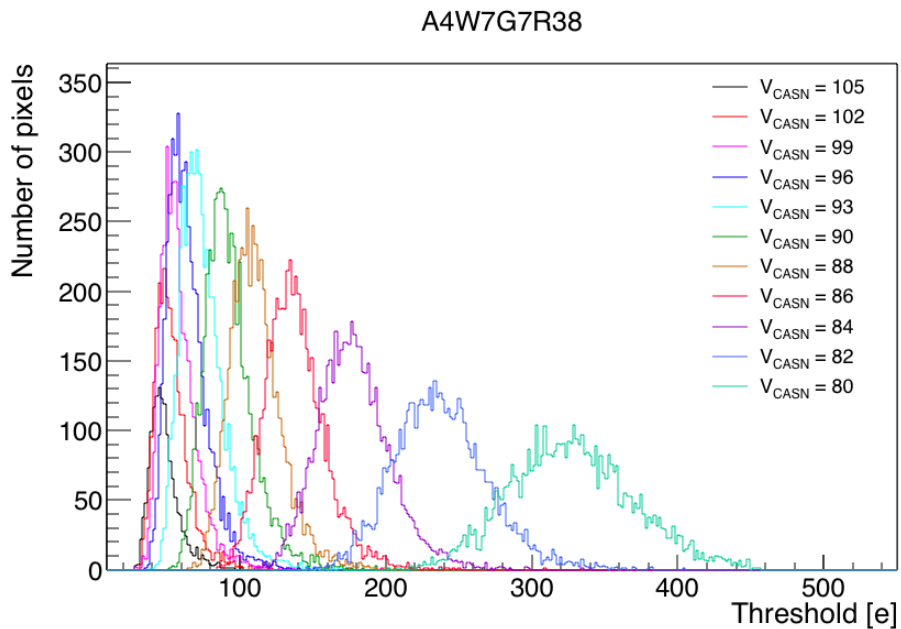


Figure 4.13: Distributions of charge threshold in pixels for different V_{CASN} settings for the chip A4W7G7R38. The measurement was done before the November 2017 irradiation. With increasing V_{CASN} the number of pixels where the fit converged increases.

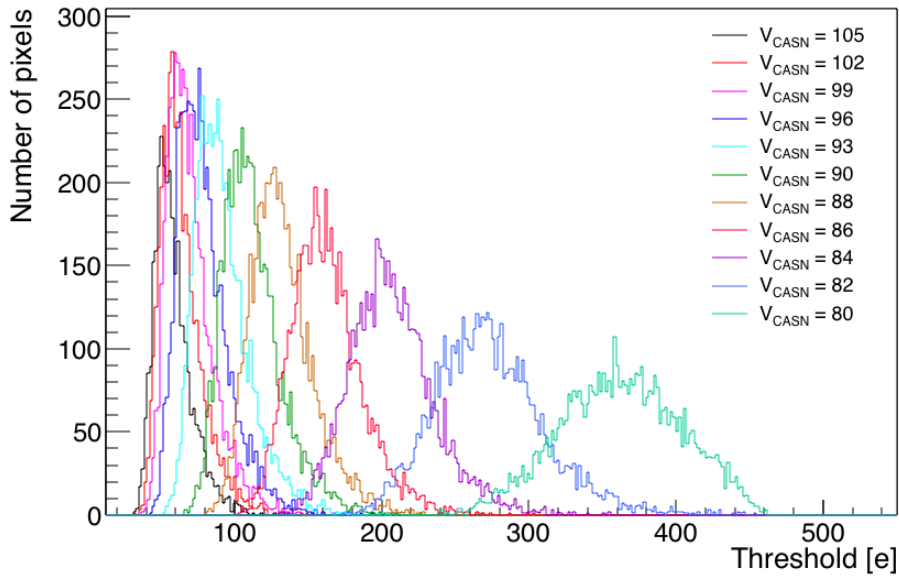


Figure 4.14: Distributions of charge threshold in pixels for different V_{CASN} settings for the chip A4W7G7R41. The measurement was done before the November 2017 irradiation. With increasing V_{CASN} the number of pixels where the fit converged increases.

4.3 The analysis of I_{THR} and V_{CASN}

The charge threshold depends on the actual I_{THR} and V_{CASN} settings. I have investigated how is the linearity of these DACs influenced by the total accumulated dose. This can be illustrated by Figures 4.15 and 4.16 which show dependencies at the beginning of each irradiation campaign. V_{CASN} remains linear during all irradiation campaigns and we can thus conclude that it is radiation hard. On the other hand, I_{THR} is affected by the accumulated dose. It keeps staying linear only until $\text{DAC} = 51$, which is the working point of the sensor, and then the linearity breaks down. From the plots, we can nevertheless see that I_{THR} shows annealing from campaign to campaign.

As was said at the beginning of the chapter, two tested chips had different radiation rates in the first irradiation campaign that took place in the September 2016: the chip A4W7G7R41 was irradiated slowly and A4W7G7R38 was irradiated three times faster. The aftermath of this fact is perfectly shown in the difference of the currents I_{THR} behavior during the first irradiation. The dependences of the I_{THR} on the DAC were measured several times during this campaign and they are shown in Fig. 4.17 and 4.18. In the case of the chip A4W7G7R38, the linearity of I_{THR} changes after the working point ($\text{DAC} = 51$) and after obtaining the dose of ~ 200 krad breaks down. However, after one month of annealing, the current be-

comes linear again. For the chip A4W7G7R41 the curves are almost the same, only the last scan of I_{THR} demonstrates a deviation from the initial trend. From Fig. 4.19 and 4.20 it is seen, that the voltage V_{CASN} in different scans does not change.

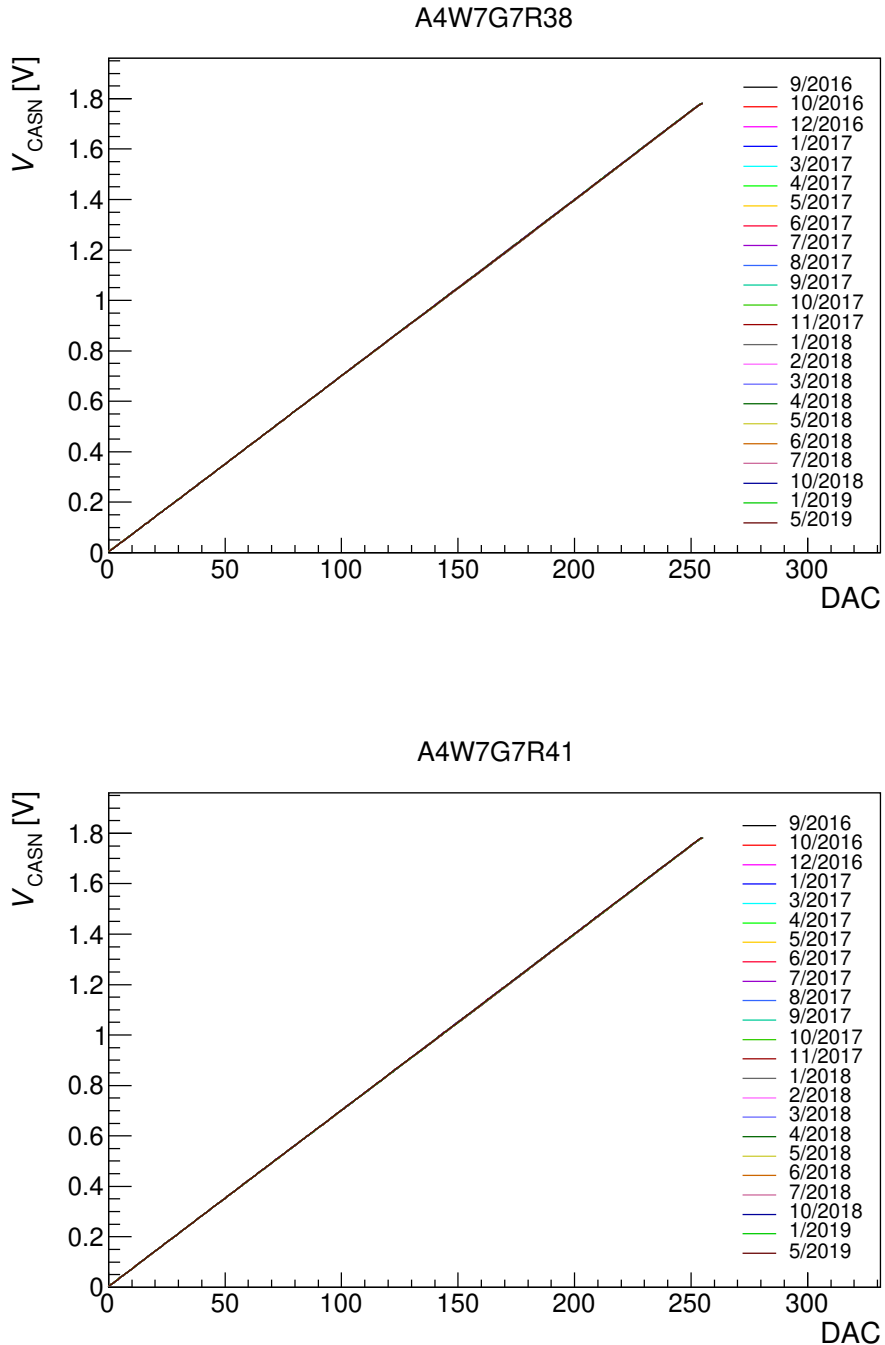


Figure 4.15: Dependence of V_{CASN} on DAC for the chips A4W7G7R38 and A4W7G7R41, measured before the start of every irradiation. The corresponding doses are in the Tab. 4.1 and Tab. 4.2.

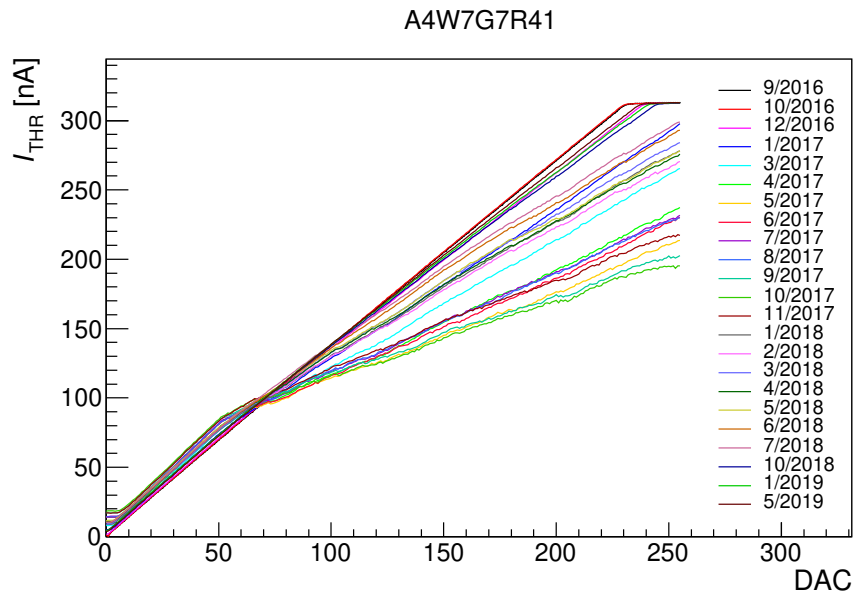
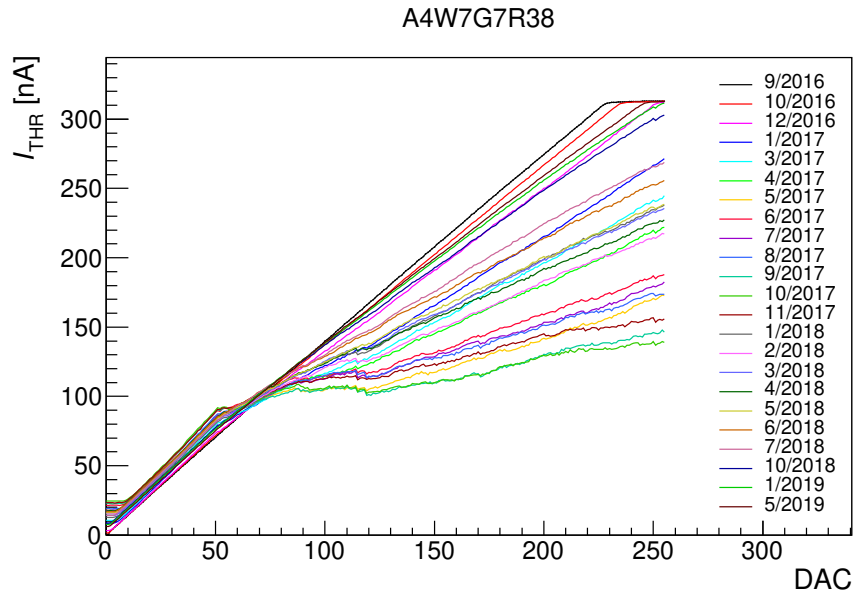


Figure 4.16: Dependence of I_{THR} on DAC for the chips A4W7G7R38 and A4W7G7R41, measured before the start of every irradiation. The corresponding doses are in the Tab. 4.1 and Tab. 4.2.

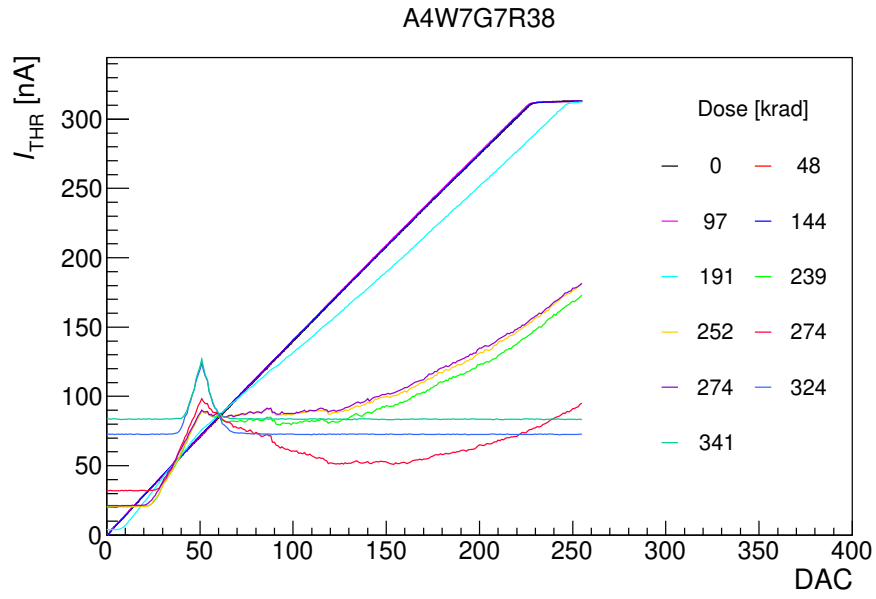


Figure 4.17: I_{THR} vs. DAC for the chip A4W7G7R38. Data are taken from the first irradiation campaign in September 2016. Different scans are marked by different colors.

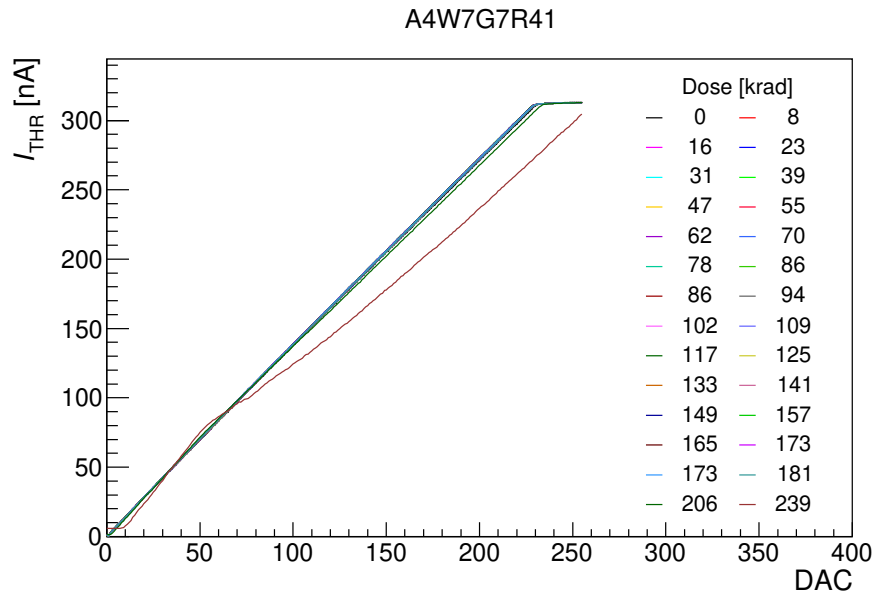


Figure 4.18: I_{THR} vs. DAC for the chip A4W7G7R41. Data are taken from the first irradiation campaign in September 2016. Different scans are marked by different colors.

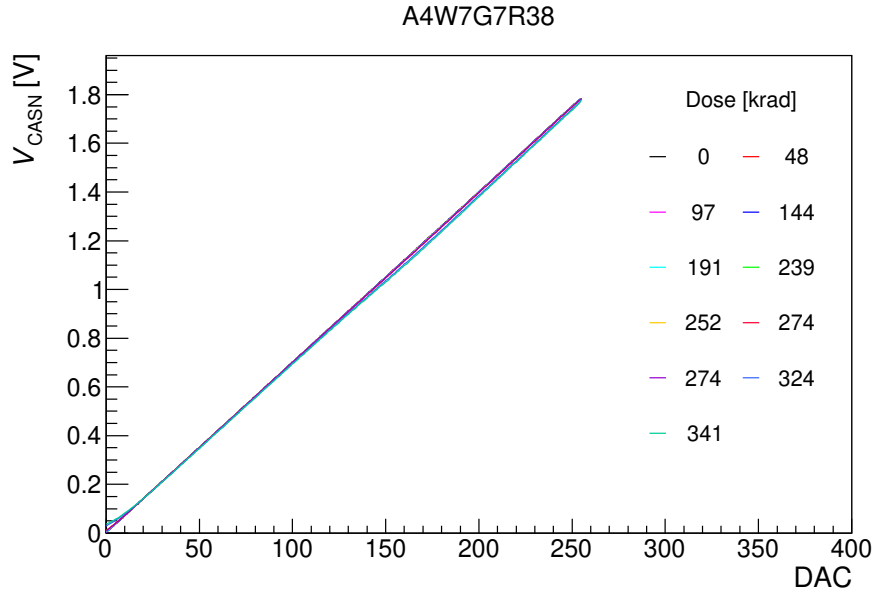


Figure 4.19: V_{CASN} vs. DAC for the chip A4W7G7R38. Data are taken from the first irradiation campaign in September 2016. Different scans are marked by different colors.

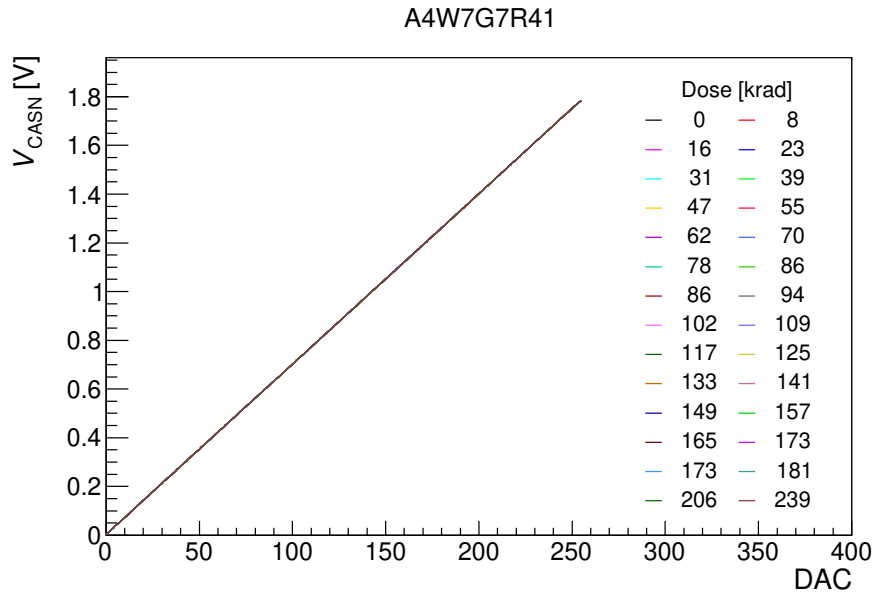


Figure 4.20: V_{CASN} vs. DAC for the chip A4W7G7R41. Data are taken from the first irradiation campaign in September 2016. Different scans are marked by different colors.

The following figures 4.21–4.22 show the behavior of the supply currents for the analog and digital circuit parts of the tested chips. In Fig. 4.21 the dependences of the analog supply current on the TID for the chips A4W7G7R38 and A4W7G7R41 in different irradiation campaigns are shown.

According to these graphs, the analog supply current decreases with the increasing obtained dose. In each campaign, irradiations were terminated when the analog supply current reached half of its initial value in order to prevent irreversible destruction of the sensor. However, after a month of annealing, the analog supply current value gets back to the range of 10–13 mA. The digital supply current remains relatively stable and varies in the range of 79–83 mA, see Fig. 4.22.

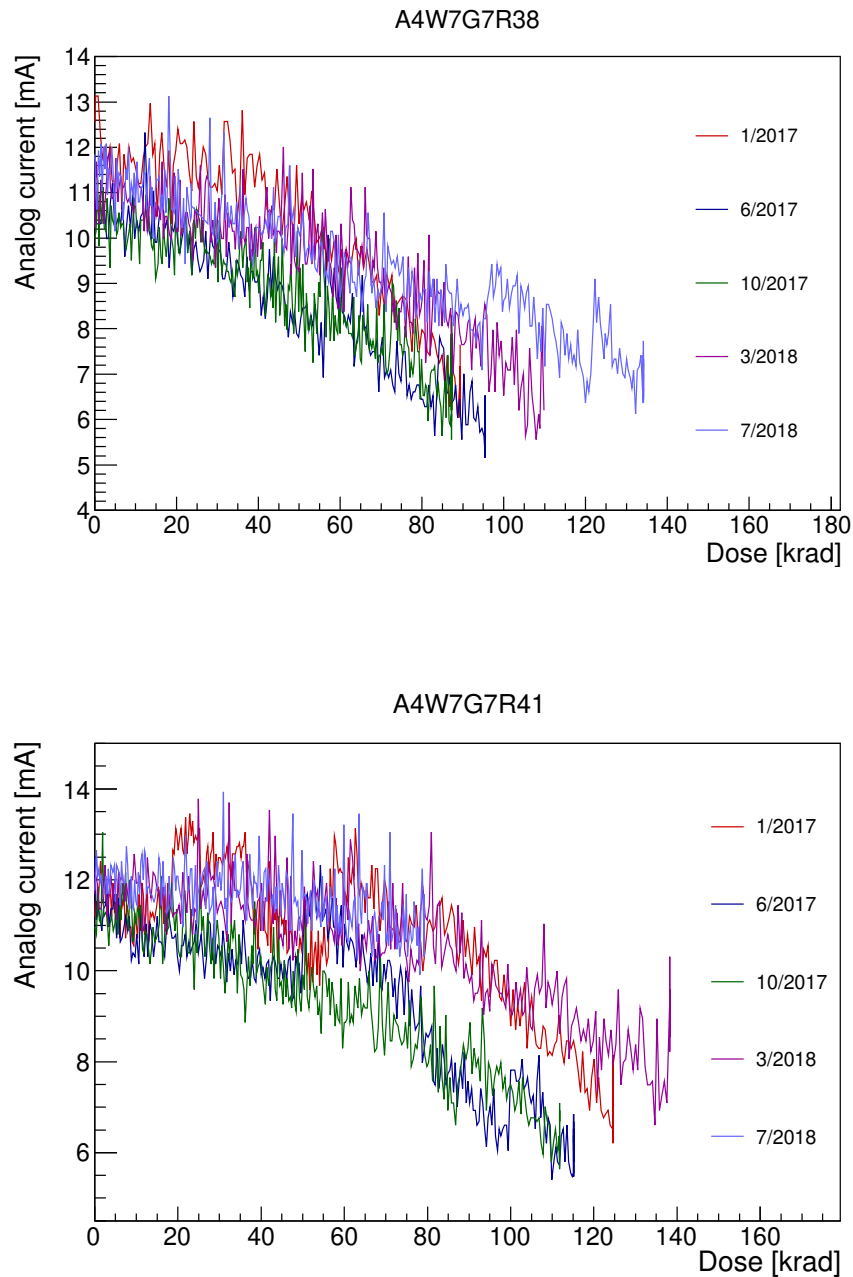


Figure 4.21: Dependence of the analog current on the TID for the chips A4W7G7R38 and A4W7G7R41 measured for different irradiation campaigns.

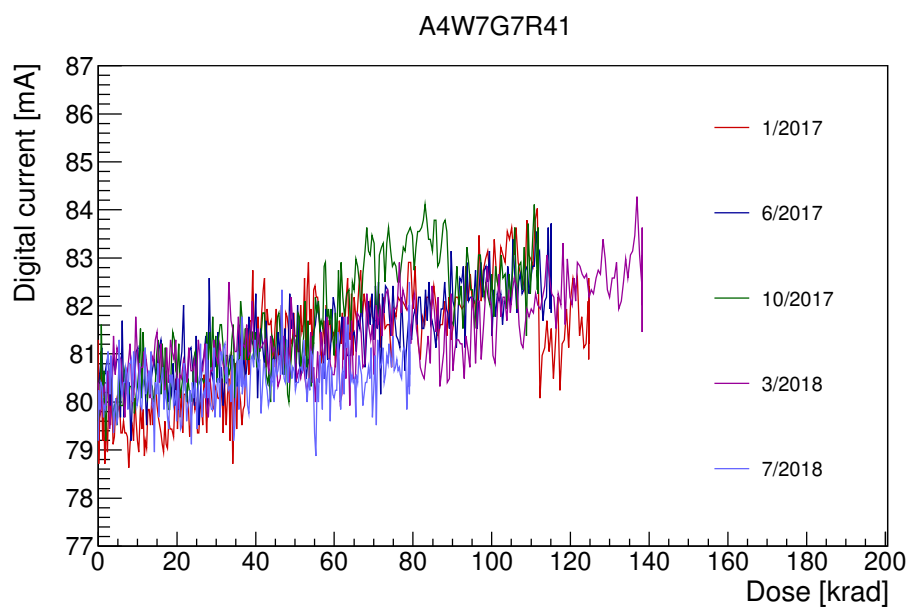
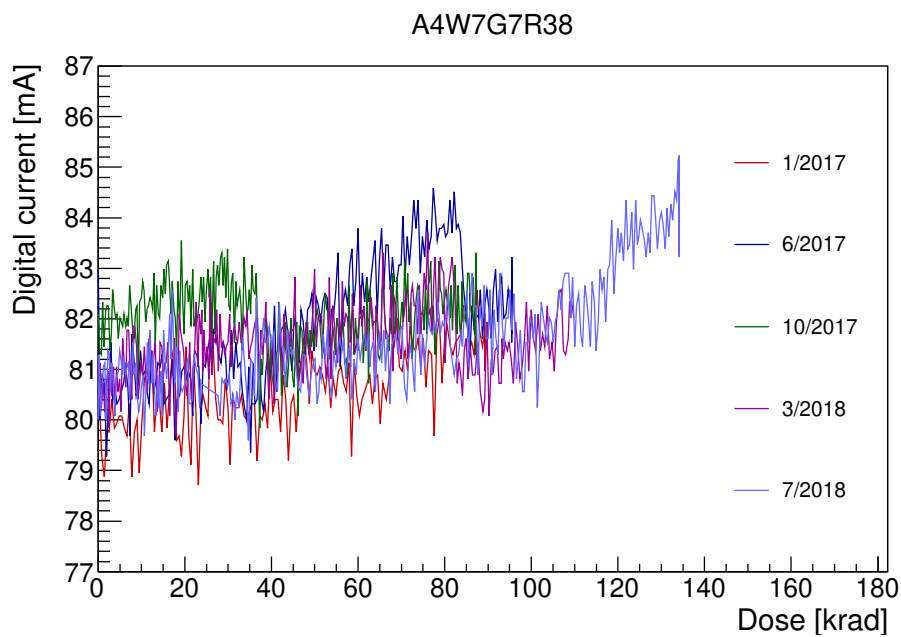


Figure 4.22: Dependence of the digital current on the TID for the chips A4W7G7R38 and A4W7G7R41 measured for different irradiation campaigns.

4.4 Fake-hit rate

One of the most important characterization parameters of the chip is its fake-hit rate, which is defined as the average number of pixels, which fired without an external stimulus N_f , normalized by the number of pixels in the chip N_p and the number of events N_e :

$$\text{Fake-hit rate} = \frac{N_f}{N_e N_p}. \quad (4.4)$$

The technical design report [8] requires that the fake-hit rate of ALPIDE is lower than 10^{-6} hits/event/pixel. Fake-hit rate was measured in the period when the chip was not irradiated and left to trigger randomly. After that I monitored which pixels fired. The measurement was provided by the macro NoiseOccupancyScan.C for 10^6 events. The higher the threshold in the chip, the lower the fake-hit rate, see Fig. 4.23, which shows such dependence made without the 10 noisiest pixels for the chips A4W7G7R38 and A4W7G7R41 in October 2018. At the time the chip A4W7G7R38 obtained the TID of 2390 krad and the NIEL of 2383×10^{10} 1 MeV n_{eq} cm^{-2} and the chip A4W7G7R41 obtained the TID of 2821 krad and the NIEL of 2813×10^{10} 1 MeV n_{eq} cm^{-2} .

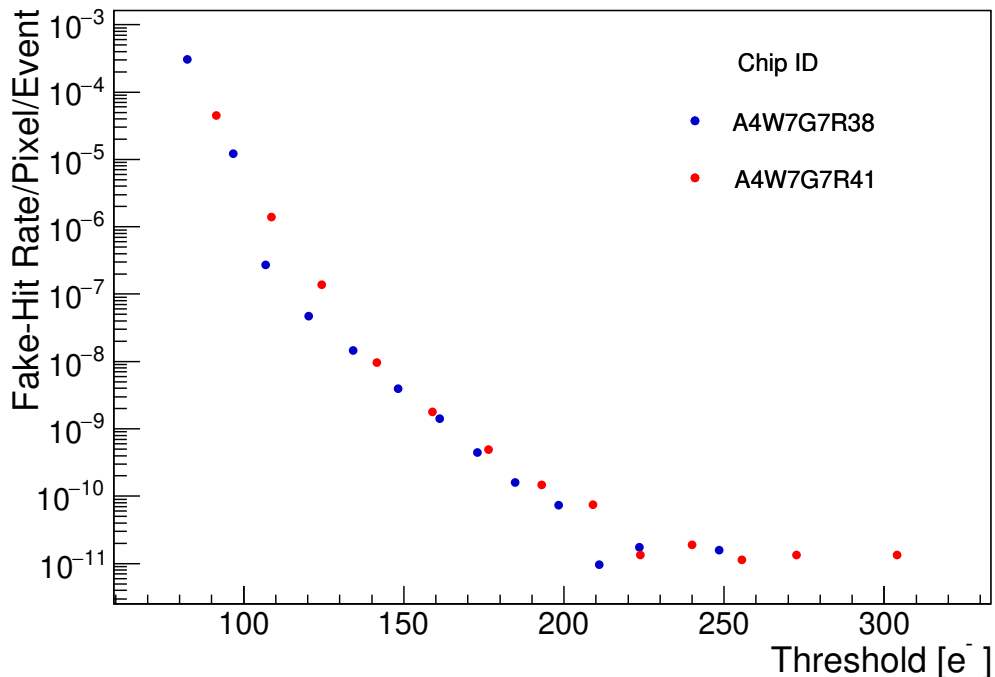


Figure 4.23: The comparison of the fake-hit rates for the chips A4W7G7R38 (blue points) and A4W7G7R41 (red points) as a function of the threshold value. In all cases, the 10 noisiest pixels were excluded.

Alternatively, we can have a look at the dependence of the fake-hit rate on

the number of excluded noisiest pixels for different thresholds. Those dependencies are shown in Fig. 4.24, 4.25 and Fig. 4.26 for the chips A4W7G7R38, A4W7G7R41 and the non-irradiated sensor, respectively. On the top panels of Fig. 4.24 and 4.25, it is seen that the number of pixels that have to be excluded to reach certain fake-hit rate level decreases. This number significantly drops when the threshold reaches 148 e in the case of the chip A4W7G7R38 and 159 e for the chip A4W7G7R41. The bottom panels of Fig. 4.24 and 4.25 show the same distribution for high threshold values only. For comparison, we show the same distribution also for the non-irradiated chip, where we had to remove just a single pixel to fulfill the project proposal limit, see Fig. 4.26. In the case of the non-irradiated sensor the number of fired pixels is small (max. 14).

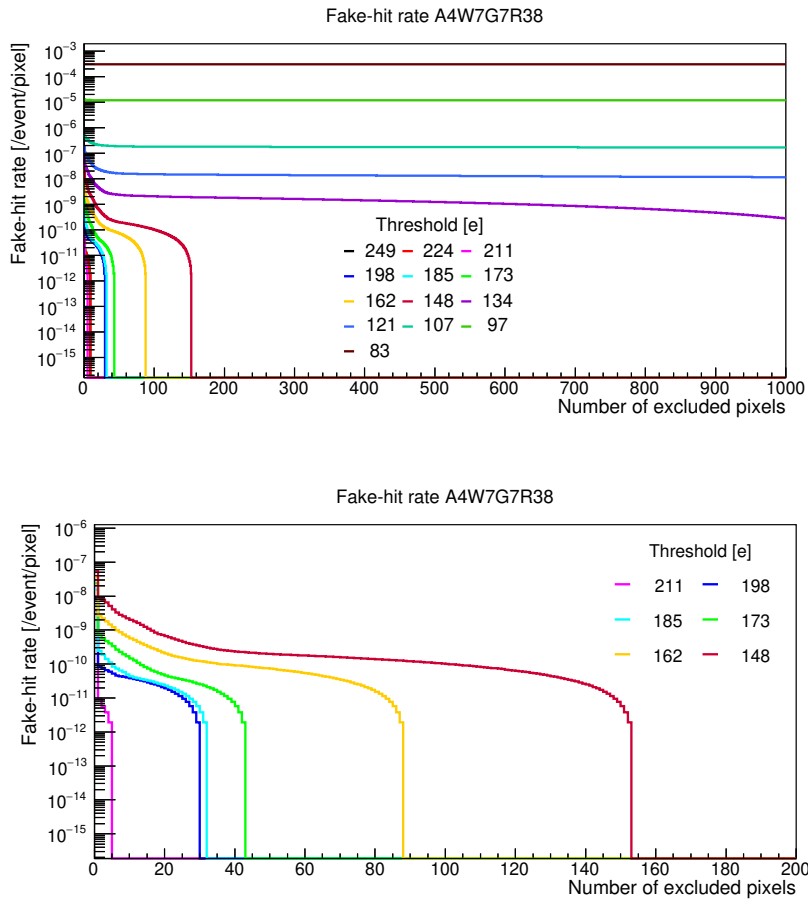


Figure 4.24: Fake-hit rate as a function of the number of excluded pixels, which were the noisiest, for the chip A4W7G7R41 for different threshold settings. At the top: Data for all thresholds. At the bottom: Data for high thresholds only. The obtained TID is 2390 krad and the NIEL is 2383×10^{10} $1 \text{ MeV n}_{\text{eq}} \text{ cm}^{-2}$.

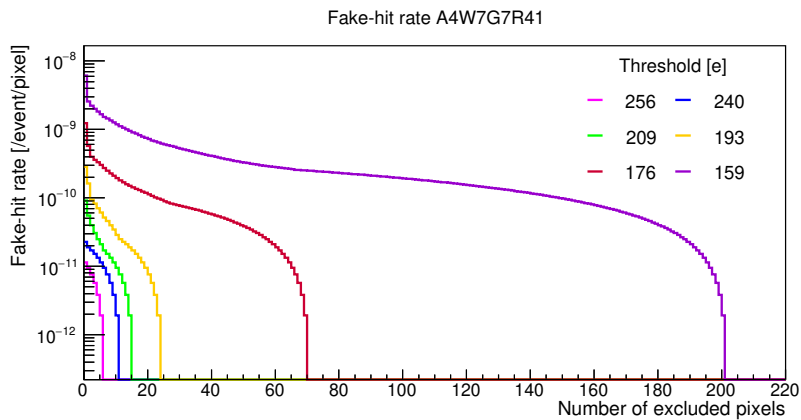
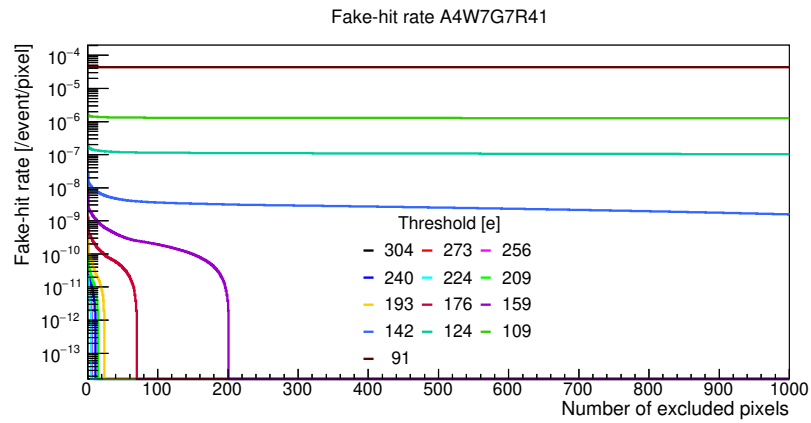


Figure 4.25: Fake-hit rate as a function of the number of excluded pixels, which were the noisiest, for the chip A4W7G7R41 for different threshold settings. At the top: Data for all thresholds. At the bottom: Data for high thresholds only. The obtained TID is 2821 krad and the NIEL is 2813×10^{10} 1 MeV n_{eq} cm^{-2} .

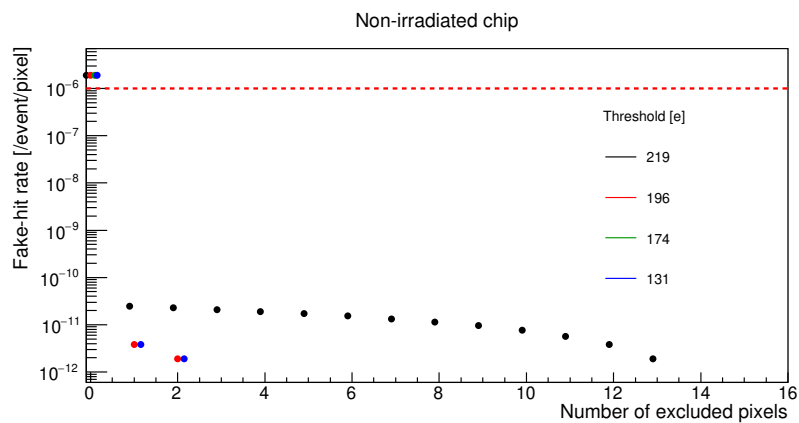


Figure 4.26: Fake-hit rate as a function of the number of excluded (the noisiest) pixels for the non-irradiated sensor for different threshold settings. The red dashed line shows the project limit on fake-hit rate.

The noise maps for different threshold settings in both chips are shown in Fig. 4.27 and 4.28. The distribution of the fake-hit rate is more or less uniform across the whole chip. With the increasing threshold, some areas of the chip become less noisy, in particular, the right-hand side part. One might think that the reason could be in the not precise placing of the chip in the center of the proton beam during the irradiation. However, the observed asymmetry is too big to be explained only by the wrong placing of the chip. The displacement would have to be significantly larger than 1 mm which we think is our precision with which we are able to place the sensor to the beam center. Therefore, we cannot exclude that the asymmetry originates from production. In the future, we plan to make a more detailed measurement of the most sensitive place along the ionization chamber using the detector Timepix. Until now it was supposed that the most sensitive part of the chamber is at its center. In addition, I also show the projection of the hit maps on the x axis for both chips, see Fig. 4.29 and Fig. 4.30.

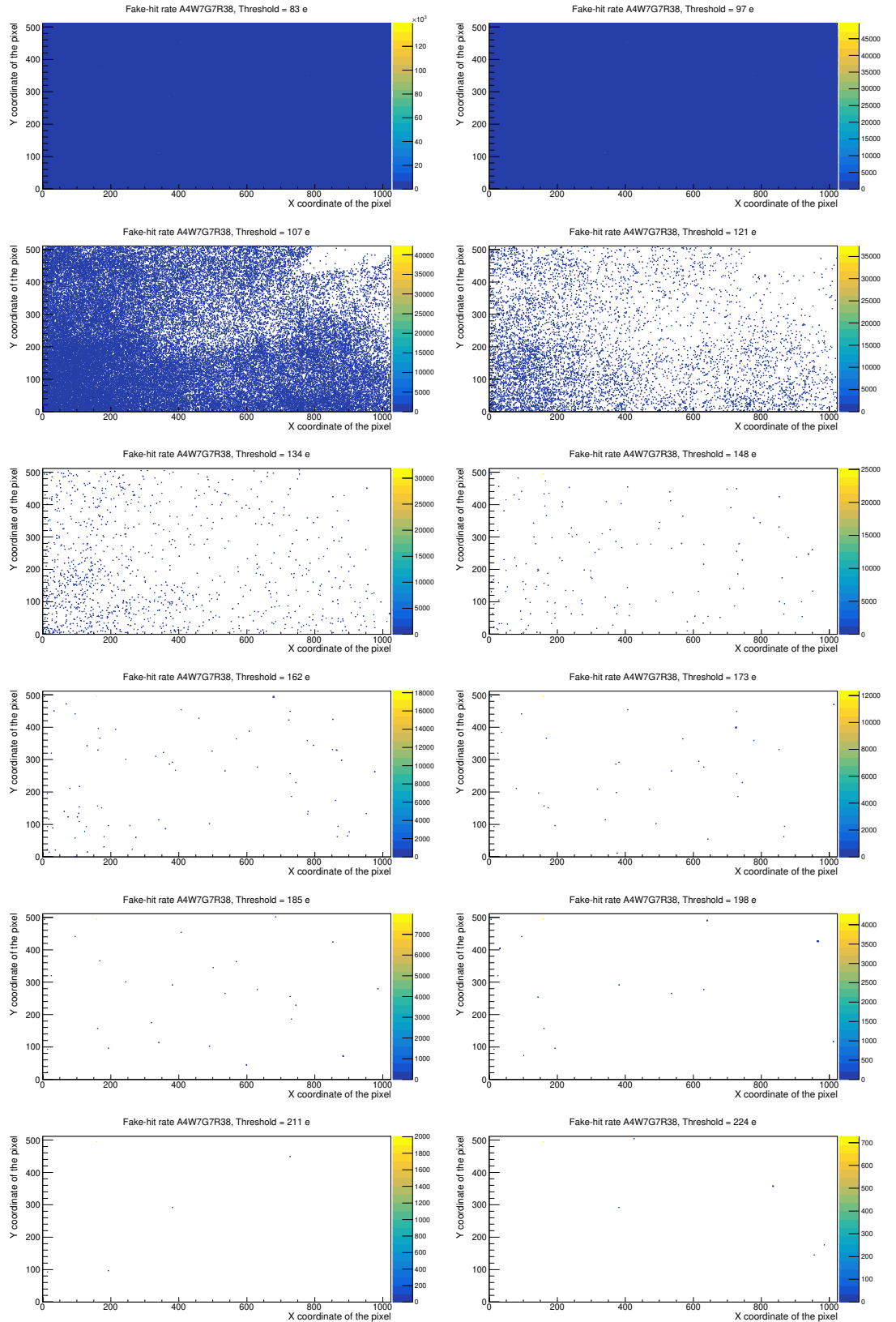


Figure 4.27: Fake-hit rate map for the chip A4W7G7R38 for different Threshold settings. The vertical and horizontal axes show x and y coordinates of the pixel on the chip and the z axis shows how many times pixel detected a signal out of 1 million trials. The obtained TID is 2390 krad and the NIEL is $2.383 \times 10^{13} \text{ 1 MeV n}_{\text{eq}} \text{ cm}^{-2}$.

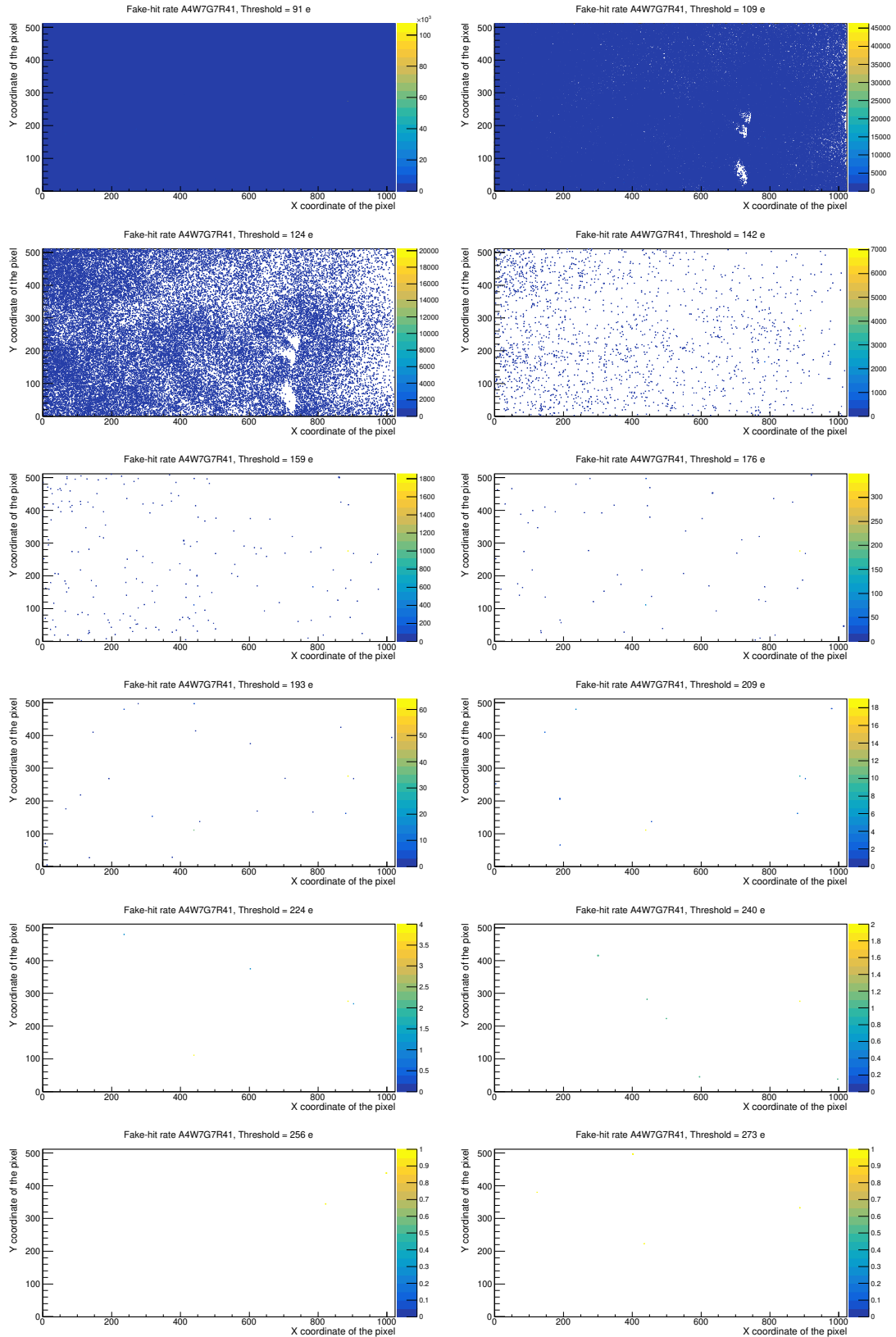


Figure 4.28: Fake-hit rate map for the chip the A4W7G7R41 for different Threshold settings. The vertical and horizontal axes show x and y coordinates of the pixel on the chip and the z axis shows how many times pixel detected a signal out of 1 million trials. The obtained TID is 2821 krad and the NIEL is 2.813×10^{13} $1 \text{ MeV n}_{\text{eq}} \text{ cm}^{-2}$.

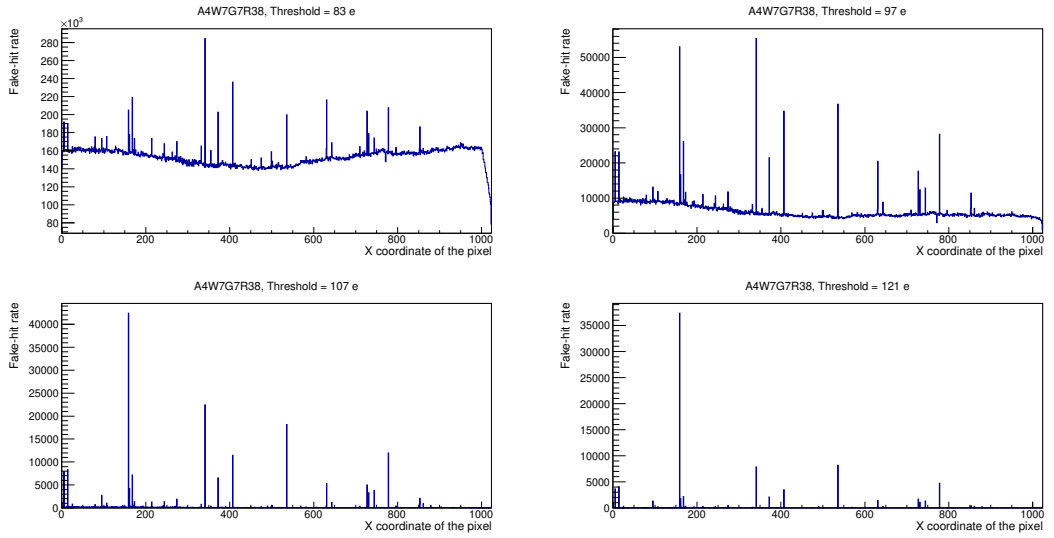


Figure 4.29: The x projection of the fake-hit rate map for the chip A4W7G7R38 for different Threshold settings. The obtained TID is 2390 krad and the NIEL is 2.383×10^{13} $1 \text{ MeV n}_{\text{eq}} \text{ cm}^{-2}$.

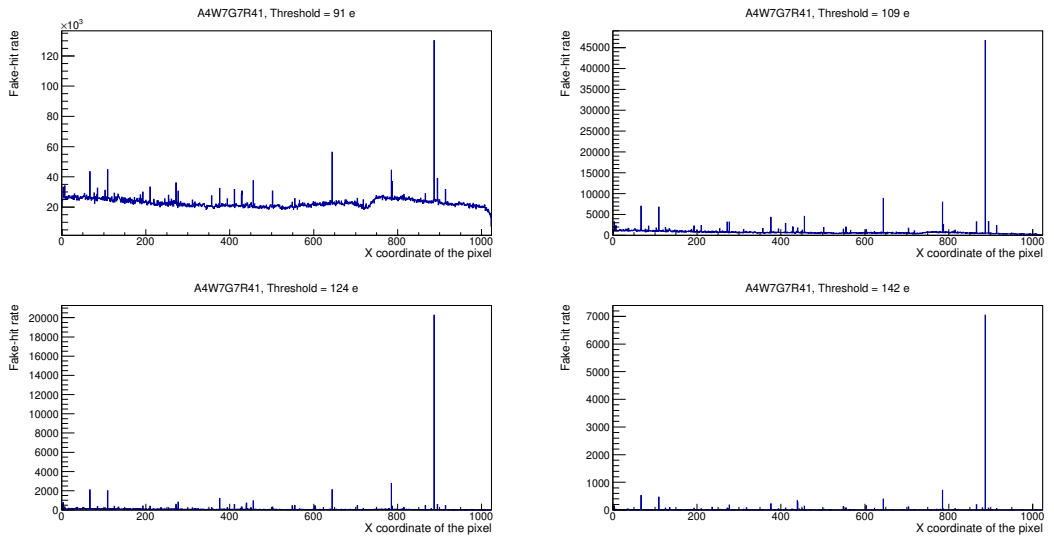


Figure 4.30: The x projection of the fake-hit rate map for the chip A4W7G7R41 for different Threshold settings. The obtained TID is 2821 krad and the NIEL is 2.813×10^{13} $1 \text{ MeV n}_{\text{eq}} \text{ cm}^{-2}$.

4.5 Characterization of the irradiated chip

After the chip A4W7G7R41 obtained the total ionizing dose of 2700 krad and the NIEL of 2.7×10^{13} $1 \text{ MeV n}_{\text{eq}} \text{ cm}^{-2}$, it was sent for the character-

ization to the CERN Proton Synchrotron. There the ALPIDE was tested using a 6 GeV/ c pion beam.

4.5.1 The setup for the CERN PS test beam

A scheme and a photo of the experimental setup used for this test is shown in Fig. 4.31 and 4.32. The setup has a form of a telescope consisting of 7 planes of ALPIDE sensors. The tested ALPIDE (device under test, DUT) was installed in the middle plane of the telescope, the other ALPIDEs served as reference planes for pion track reconstruction. The reconstructed track is used for extrapolation to the DUT. The extrapolated position of the hit is then compared to the one which was measured by the DUT itself. This allows studies of chip detection efficiency and position resolution.

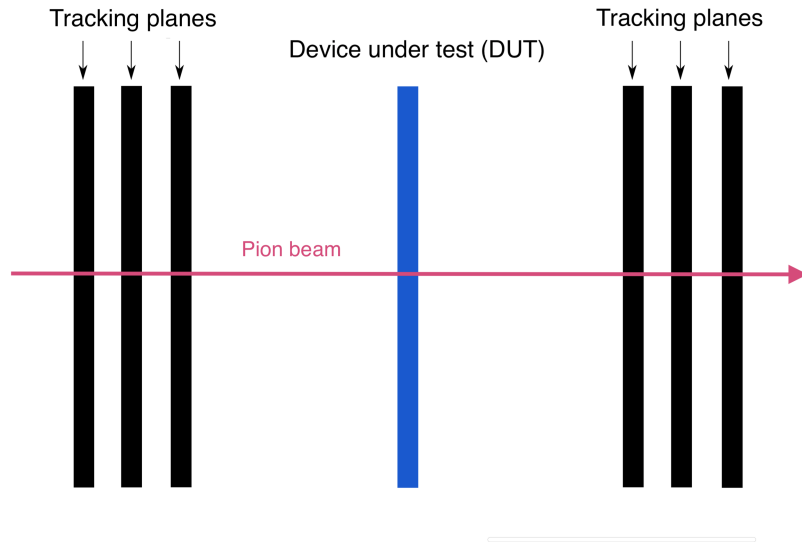


Figure 4.31: Scheme of a test beam setup that was used for ALPIDE characterization at the CERN PS. The telescope consists of 6 tracking planes (black) and the DUT (blue), a pink line shows the pion beam.

The data taking from the test-beam is performed by the EUDAQ framework [44]. I have analyzed these data using the software framework EUTelescope [45]. This framework uses special libraries and functions for telescope data analysis. The analysis proceeds in several steps:

- **converter**
In this step the data after data-taking are converted to a suitable format for the framework, the format *lcio* (Linear Collider Input Output).
- **deadColumn**
Sometimes during the data - taking it appears that a double column of pixels is deactivated. This may be caused by a faulty pixel. In this

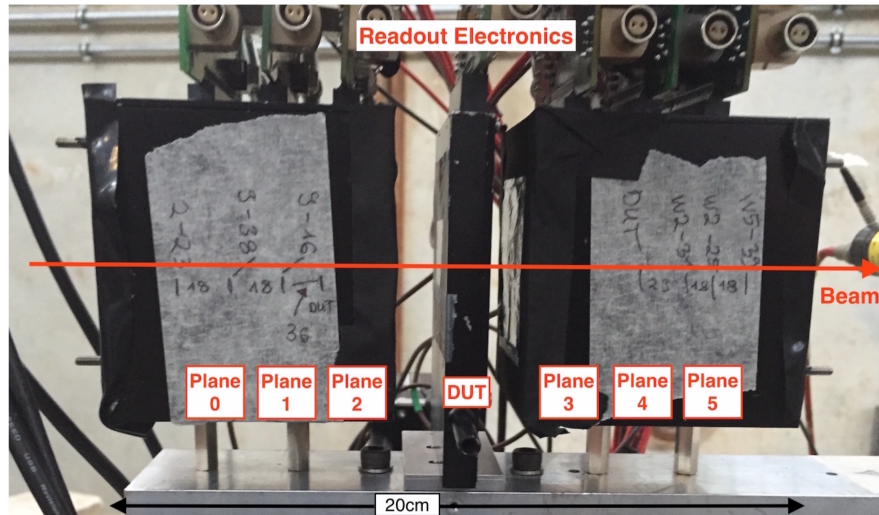


Figure 4.32: Photo of the data taking setup consisting of 6 reference ALPIDEs and the tested one in the middle, taken from [46].

step, such dead columns are found and flagged. The signals from those parts of the chip are excluded from the efficiency calculation, in order not to underestimate artificially the real efficiency values.

- **hotpixel**

This step identifies and removes too noisy or faulty pixels. It is investigated how often each pixel fires during the first 10 000 events and if it exceeds a certain limit, then such a pixel is declared as noisy and the closest tracks and clusters are ignored in further process. This step is done twice with two different limits: when doing the alignment of the detector planes when a strict limit is applied and later when doing the efficiency when a looser condition is applied.

- **clustering**

A charged particle passing through the detector can generate a hit in more than one pixel. This will result in a group of firing pixels placed close to each other, such a group is called a cluster. The distance between pixels, which may be considered as a cluster, can be set. This step identifies such clusters by grouping pixels which fired in the same event.

- **hitmaker**

This step calculates the center of gravity for clusters found in the previous step. After this step, each cluster is associated with the definite x , y and z coordinates (of its center of gravity). After this, the calculated coordinates undergo the transformation from the chip local coordinate system to the global coordinate system, where the point $(0,0,0)$ corresponds to the center of the first chip. The initial parameters for transformation between coordinate systems are contained in a so-called gear file, which is unique for every test-beam campaign and also includes the information of the material budget of the telescope

layers. The parameters that describe the orientation and the position of the plates are then defined more precisely by the subsequent alignment.

– **prealign**

After the coordinates transformation, the alignment of the planes follows. The alignment consists of 2 steps: prealign and align. These steps make the correction for the planes positioning since our determination of planes' coordinates is not perfect. During the prealignment we calculate the distance in x and y between the hit positions in the first plane and all other planes. Then it calculates how much the mean of this distribution differs from 0 for all planes.

– **align**

The prealignment results are applied to the data and more precise alignment can be calculated. This step uses straight tracks, where the first and the last planes are treated as fixed. The alignment correction is then calculated using χ^2 minimization. This step fits three parameters for each plane: the shift in x , the shift in y and the shift in z . The example of the align step output in x and y axes for the DUT is shown in Fig 4.33.

– **fitter**

This step applies prealignment and alignment to the hits and fits the tracks. The hits in the DUT are not included in the fitting, because its detection efficiency and resolution should be studied. The impinging point of the track at the DUT is also calculated in this step. Tracking has to take into account the material budget of the tracking planes and uses a piecewise linear function, where the angle is determined by the multiple scattering.

– **analysis**

In this step the association between DUT impinging points and extrapolated tracks is made. The mean values of such residuals for different I_{THR} are presented in Fig. 4.34. The detection efficiency and spatial resolution are then calculated. Also, the size and shape of the clusters are investigated.

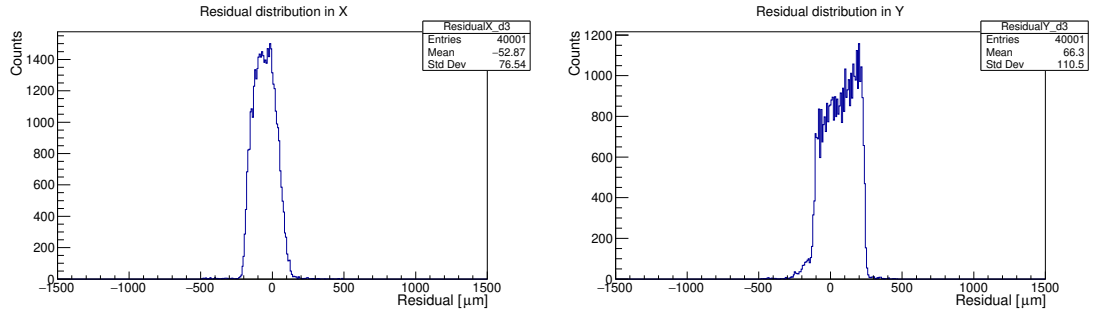


Figure 4.33: The residual distribution in x (left panel) and y (right panel) axes of the chip A4W7G7R41 with $I_{\text{THR}} = 51$ DAC units obtained in the align step.

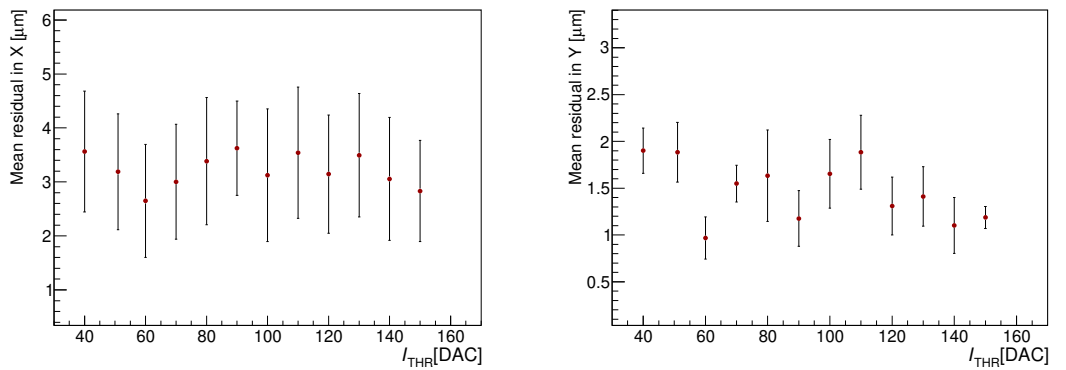


Figure 4.34: The mean residuals in x (left panel) and y (right panel) axes of the chip A4W7G7R41 for different I_{THR} obtained in the analysis step.

The result of the characterization is presented in Fig. 4.35 and in Fig. 4.36. Figure 4.35 shows the dependence of detection efficiency (black markers) and the fake hit rate (red markers) on the mean charge threshold for the irradiated chip and for a non-irradiated reference chip. The fake-hit rate data presented in Fig. 4.35 show the values after excluding the 10 noisiest pixels. The black dash-dotted line corresponds to the project limit on detection efficiency which should be higher than 99% and the red dash-dotted line gives the limit on the fake-hit rate which is 10^{-6} /pixel/event. In the threshold range 150–200 electrons, the measured fake hit rate of the chip A4W7G7R41 (red data) stays below the project limit and its detection efficiencies (black data) are above the project limit, so we can conclude that the irradiated sensor still fulfills the requirements of the upgrade project in terms of detection efficiency and fake hit rate. On the other hand, the non-irradiated sensor is much less noisy and falls below the efficiency limit only above the threshold value of 250 electrons. Figure 4.36 shows the resolution (black markers) and the average cluster size (red markers) for the irradiated chip A4W7G7R41 and the non-irradiated sensor vs. mean charge threshold. For the threshold higher than ~ 150 electrons the position resolution values

are slightly higher than the project limit and the cluster sizes are lower than the project limit.

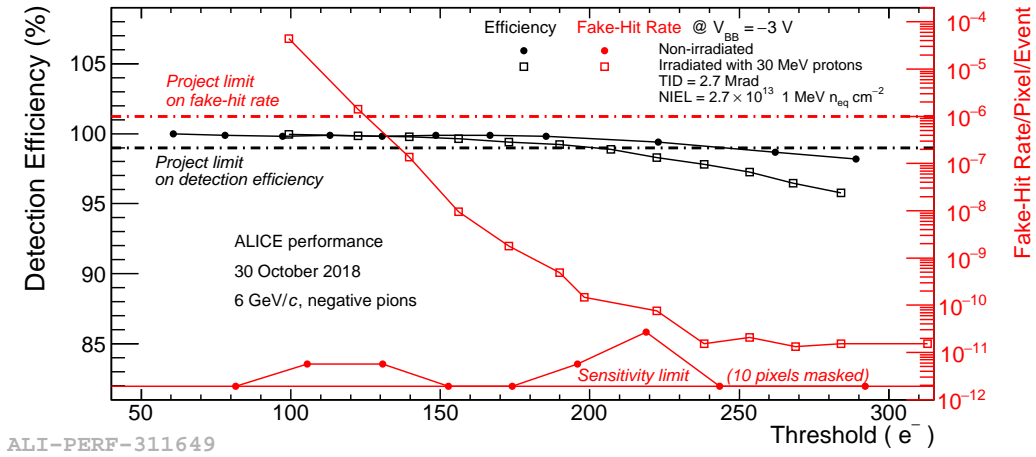


Figure 4.35: The dependence of efficiency and fake-hit rate on mean charge threshold value for the irradiated chip (A4W7G7R41) and a non-irradiated chip [40], [47].

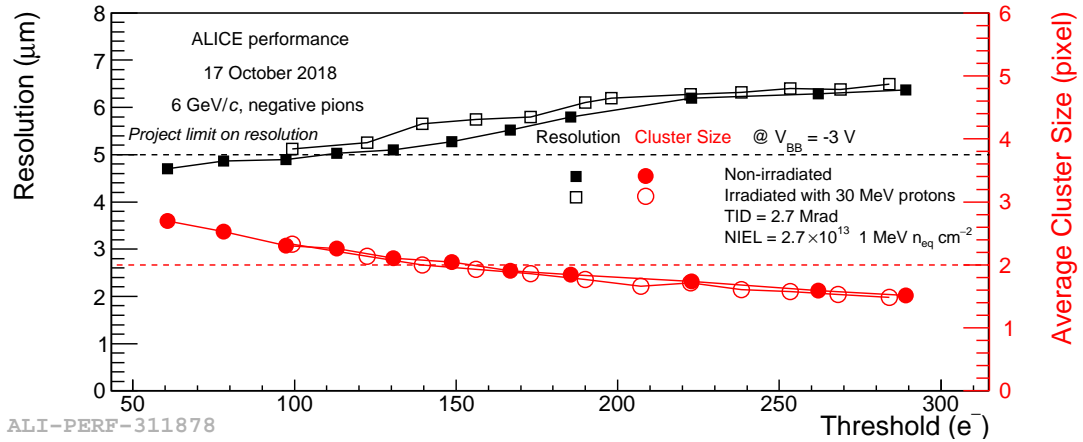


Figure 4.36: The dependence of resolution and average cluster size on mean charge threshold value for the irradiated chip (A4W7G7R41) and a non-irradiated chip. Taken from [47].

Chapter 5

ALICE ITS Commissioning

Before being installed in the ALICE cavern in July 2020, the new ITS is undergoing the on-surface commissioning. For these purposes, the whole system that will be used in the real experiment (including powering, cooling, full readout chain etc.) was placed in a special clean room at CERN. All staves of the inner barrel (IB) and the outer barrel (OB) are currently integrated into Half-Barrels and connected to the services for the tests. The Detector Control System (DCS) together with the Data-Acquisition system (DAQ) responsible for detector monitoring and data flow are running on the machines placed in a control room abutting to the cleanroom.

Since May 2019 the detector has been kept running and the collection with the acquisition of data (threshold scans, fake hit rate scans etc.) had begun. Shift crews continuously control the status of the power and the cooling from the control room. Shifters have at their disposal two PCs: one for detector monitoring and another one for data-taking and data Quality Control (QC). The status of the layers is monitored on the three different panels corresponding to the three ITS sections (inner layers of the IB, middle layers of the OB and outer layers of the OB). Each panel shows a geometrical representation of the layers, representing the detailed information about every single stave, see Fig. 5.1 (left). Staves are coloured according to their state (Power units OFF/ON, monitoring enabled, stave powered, temperature alarm etc.). Other available panels are the "Trends panels", showing the trending plots of power unit and stave temperature, analogue and digital voltage/current Fig. 5.1 (right) and the "Safety status overview panel", giving us a general overview of the detector safety. Last but not least, "Run control panel" controls the running of the tests and data taking to monitor the performance of the detector. Shifters must run a Threshold scan, a Fake-hit Rate scan, and a Readout test every hour and carry out also other tests required by experts. The configurations of the tests are set by experts. Outputs of these runs are subsequently processed by the QC framework. The runs and detector state are logged in a dedicated collaboration Logbook.

I have actively participated in 43 ITS commissioning shifts since May 2019 and have learned a lot about the detector operation, see Fig. 5.2. More

information about ITS construction and commissioning may be found in [48].

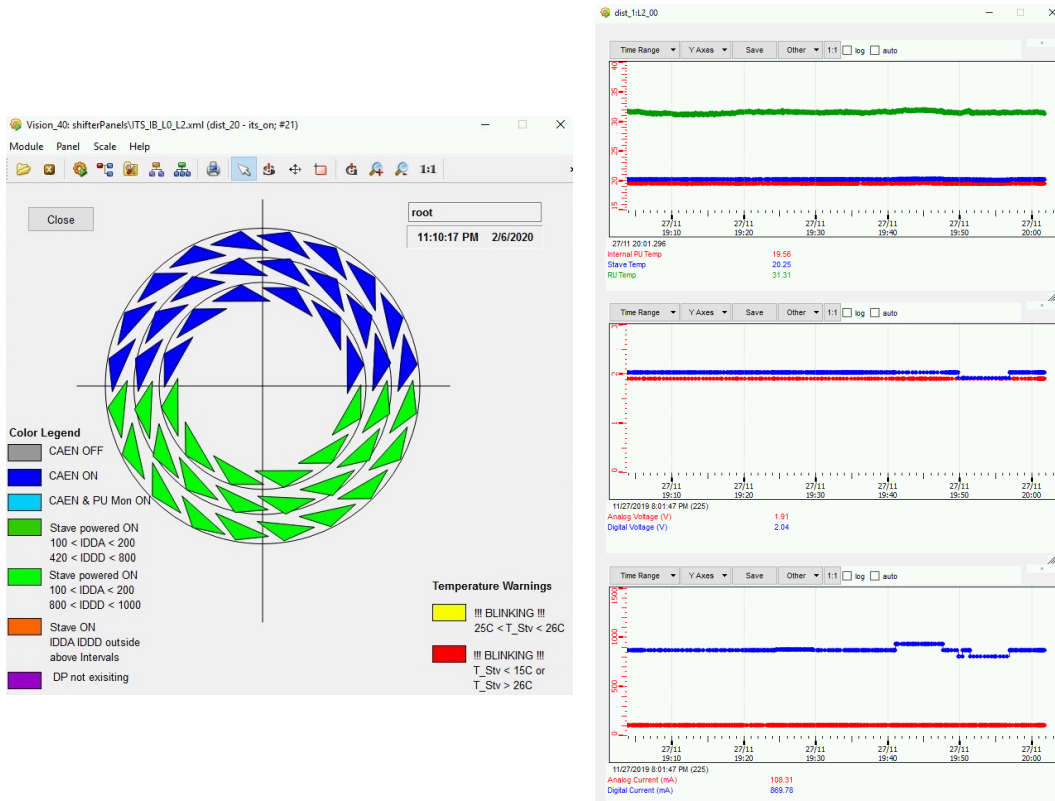


Figure 5.1: The screenshots of the detector information panels, taken from ALICE ITS Commissioning Log book. Left: the status of the IB layers. The power and readout units of all the top half barrel staves are powered on, but not monitored. The chips of the bottom half barrel staves are configured and collecting data. Right: the trends of temperature, analogue and digital current and voltage of the layer 2.



Figure 5.2: ALICE ITS Commissioning shift in October 2019.

Conclusion

In this thesis, I report the radiation hardness tests of the ALPIDE sensors. The ALPIDE sensors are intended to be used in the upgrade of the ALICE Inner Tracking System. Because the ALPIDE chip should sustain radiation loads up to 2700 krad, it is necessary to study its radiation hardness. Such tests were carried out at the U-120M cyclotron of the Nuclear Physics Institute of the Czech Academy of Sciences in Řež. The tests were performed for two chips, labeled A4W7G7R38 and A4W7G7R41. The status from June 2019 is the following: the chip A4W7G7R41 successfully sustained the radiation load of 2821 krad and was already characterized and the chip A4W7G7R38 sustained the required radiation load of 2700 krad. We see that on average the A4W7G7R38 was able to absorb less dose during irradiation campaigns than the chip A4W7G7R41. We expect that this behavior is a consequence of the different dose rates which were used for irradiation during the first campaign. Further, we have seen that for the initial settings of the ALPIDE DACs, the mean threshold decreased with the total accumulated dose while the average temporal noise increased. After retuning of thresholds by applying the new VCASN settings in November 2017 we observe annealing of thresholds. The data from DAC scans show that the voltage DACs do not change with the accumulated dose and remain linear. On the other hand, the current DACs break their linearity above the usual working point. The original trend is never recovered and we see only partial recovery by annealing. The chip will be further monitored to see how the annealing process affects both chips.

After the chip A4W7G7R41 got the required radiation load of 2700 krad and the NIEL of $2.7 \times 10^{13} \text{ 1 MeV n}_{\text{eq}} \text{ cm}^{-2}$ its performance was tested using the 6 GeV/ c pion beam from the CERN PS. Such characterization parameters as detection efficiency, fake-hit rate, spatial resolution and average cluster size of the irradiated chip were investigated. The analysis of those tests showed that the irradiated ALPIDE sensor still meets the project requirements.

I presented the results of this work at the 10th Czech-Slovak Student Scientific Conference in Physics, where I won the second prize. The results were also published in the Universe journal [40].

Literature

- [1] K. Aamodt (ALICE collaboration), *The ALICE experiment at the CERN LHC*, JINST 3 (2008) S08002.
- [2] L. Evans, P. Bryant (editors), *LHC machine*, JINST 3 (2008), S08001.
- [3] J. C. Collins and M. J. Perry, *Superdense matter: Neutrons or asymptotically free quarks?*, Phys. Rev. Lett., 34:1351356, May 1975.
- [4] E. V. Shuryak, *Quantum chromodynamics and the theory of superdense matter*, Physics Reports, 61(2):71158, 1980.
- [5] R. Stock, *Relativistic Nucleus-Nucleus Collisions and the QCD Matter Phase Diagram*, arXiv: 0807.1610v1 [nucl-ex] .
- [6] A. Majumder, M. Van Leeuwen, *The Theory and Phenomenology of Perturbative QCD*, Prog. Part. Nucl. Phys. 66 (2011) 41-92.
- [7] K. Aamodt et. al. (ALICE collaboration), *Charged-Particle Multiplicity Density at Midrapidity in Central Pb-Pb Collisions at $\sqrt{s_{NN}} = 2.76$ TeV*, Phys. Rev. Lett., 105, 252301(2010).
- [8] B. Abelev et al. (ALICE Collaboration), *Technical Design Report for the Upgrade of the ALICE Inner Tracking System*, J.Phys.G 41 (2014), 087002.
- [9] ALICE, *Letter of intent*, J.Phys. G41 (2014) 087001.
- [10] ALICE Collaboration (Christian Lippmann for the collaboration), *Upgrade of the ALICE Time Projection Chamber*, CERN-LHCC-2013-020, ALICE-TDR-016.
- [11] P. Antonioli, A. Kluge, W. Riegler, *Upgrade of the ALICE Readout & Trigger System*, CERN-LHCC-2013-019; ALICE-TDR-015.
- [12] ALICE general figures, https://alice-figure.web.cern.ch/general_fig, [Online 24.02.2018].
- [13] A. Alici et al, *Radiation Dose and Fluence in ALICE after LS2*, ALICE-PUBLIC-2018-012.
- [14] W. R. Leo, *Techniques for Nuclear and Particle Physics Experiments*, Springer-Verlag Berlin Heidelberg 1987, 1994.
- [15] G. Lutz, *Semiconductor Radiation Detectors*, Springer-Verlag Berlin Heidelberg 2007.
- [16] Silicon electrical properties, <http://www.ioffe.ru/SVA/NSM/Semicond/Si/electric.html>, [Online 6.09.2018].

- [17] S. N. Ahmed, *Physics and Engineering of Radiation Detection*, Elsevier 2014.
- [18] H. Spieler, *Semiconductor Detector Systems*, Oxford University Press 2005.
- [19] J. W. van Hoorne, *Study and Development of a novel Silicon Pixel Detector for the Upgrade of the ALICE Inner Tracking System*, PhD thesis, TU Vienna, Oct 2015.
- [20] STAR Collaboration, *A Heavy Flavor Tracker for STAR*, Tech. Rep. LBNL/PUB-5509-2008, 2008.
- [21] M. Moll, *Radiation damage in silicon particle detectors: Microscopic defects and macroscopic properties*, PhD thesis, Hamburg U., 1999.
- [22] E. Fretwurst, G. Lindstrom, I. Pintilie and J. Stahl, *Radiation damage in silicon detectors caused by hadronic and electromagnetic irradiation*, arXiv preprint physics/0211118 (2002).
- [23] M. Varga-Köfaragó, *Anomalous Broadening of Jet-Peak Shapes in Pb–Pb Collisions and Characterization of Monolithic Active Pixel Sensors for the ALICE Inner Tracking System Upgrade*, CERN-Thesis, 2018.
- [24] H. Hillemanns, *Radiation Hardness of Monolithic Active Pixel Sensors for the ALICE Inner Tracking System Upgrade*, CERN, CH-1211.
- [25] P. Yang et al., *Low-power priority Address-Encoder and Reset-Decoder data-driven readout for Monolithic Active Pixel Sensors for tracker system*, Nuclear Inst. and Methods in Physics Research, A785 (2015) 61–69.
- [26] Nuclear physics, MSU, <http://nuclphys.sinp.msu.ru/experiment/accelerators/ciclotron.htm>, [Online 22.07.2018].
- [27] T. Matlocha, *Soustava pro vývod kladných iontů z cyklotronu*, Study for dissertation, FJFI ČVUT, 2018.
- [28] L.H. Thomas, *The Paths of Ions in the Cyclotron I. Orbits in the Magnetic Field*, Phys. Rev. 54, 580 (1938).
- [29] Department of accelerators, Isochronous cyclotron U-120M, <http://accs.ujf.cas.cz>, [Online; accessed 19.05.2017].
- [30] Center of Accelerators and Nuclear Analytical Methods, Nuclear Physics Institute of the CAS, <http://canam.ujf.cas.cz>, [Online; accessed 11.09.2018].
- [31] F. Křížek, ... V. Raskina, ... , *Irradiation setup at the U-120M cyclotron facility*, Nuclear Inst. and Methods in Physics Research, A 894 (2018) 87–95.
- [32] T. Vaňát, *Physical Fault Injection and Monitoring Methods for Programmable Devices*, Dissertation, FIT ČVUT 2017.
- [33] User manual PTW, *Ionization Chamber Type 30010, 30011, 30012, 30013; D596.131.00/03 2006-09 Hn*, Freiburg: PTW, 2013. 16.
- [34] L. Musílek, *Úvod do fyziky ionizujícího záření*, SNTL 1979.

- [35] UNIDOS E, Universal dosimeter, http://www.ptw.de/unidos_e_dosemeter_ad0.html, [Online; accessed 10.09.2018].
- [36] V. Raskina, *Measurement of proton flux from the U-120M cyclotron using activation foils*, Bachelor's Thesis FJFI ČVUT 2018.
- [37] K. Vysoká, *Low Proton Flux Measurements at the U-120M Cyclotron for Radiation Hardness Studies*, Master's thesis, FJFI ČVUT 2016.
- [38] ESCC, *Single event effects tests method and guidelines*, ESCC Basic Specification No. 25100, October 2016.
- [39] J. F. Ziegler, J. P. Biersack, *The Stopping and Range of Ions in Matter*, Treatise on Heavy-Ion Science, pages 93–129. Springer US, 1985
- [40] V. Raskina, F. Křížek, *Characterization of Highly Irradiated ALPIDE Silicon Sensors*, Universe 5 (2019) no.4, 91.
- [41] Displacement Damage in Silicon, <https://rd50.web.cern.ch/rd50/NIEL/default.html>, [Online; accessed 28.05.19].
- [42] B. Brüers, *Analysis of testbeam data with inclined pALPIDE-3 chips*, Report of the CERN Summer Student Programme 2016.
- [43] Geant4, <https://geant4.web.cern.ch>, [Online; accessed 15.08.2019].
- [44] EUDAQ User Manual, http://eudaq.github.io/manual/EUDAQUserManual_v1.pdf, [Online; accessed 29.06.2019].
- [45] EU Telescope Documentation and Source Code, <http://eutelescope.web.cern.ch>, [Online; accessed 27.04.2019].
- [46] Felix Reidt, *Studies for the ALICE Inner Tracking System Upgrade*, CERN-Thesis, 2016.
- [47] S. Kushpil (ALICE Collaboration), *Recent results from beam tests of the ALPIDE pixel chip for the upgrade of the ALICE Inner Tracker*, IEEE Transactions on Nuclear Science, 2019.
- [48] D. Colella for the ALICE Collaboration, *ALICE Inner Tracking System Upgrade: construction and commissioning*, arXiv:1912.12188 [physics.ins-det].

Appendix

Appendix A

Dose calculation

Total ionizing dose D is estimated by formula:

$$D[\text{krad}] = 1.602 \times 10^{-8} \times \text{LET}[\text{MeV} \cdot \text{cm}^2 \cdot \text{mg}^{-1}] \times F[\text{cm}^{-2}], \quad (\text{A.1})$$

where LET is the stopping power, F is fluence. The unit test may be made in the following way. The effective unit of $\text{LET} \times F$ is $1 \frac{\text{MeV}}{\text{mg}}$, which can be written as

$$1 \frac{\text{MeV}}{\text{mg}} = \frac{10^{-6} \text{eV}}{10^{-6} \text{kg}} = 10^{12} \frac{\text{eV}}{\text{kg}} = 10^{12} \cdot \frac{e \cdot J}{\text{kg}} = 10^{12} \cdot e \cdot \text{Gy}, \quad (\text{A.2})$$

where e is elementary charge and $1 \text{ Gy} = 0.1 \text{ krad}$. Which leads to

$$1 \frac{\text{MeV}}{\text{mg}} = 10^{12} \cdot e \cdot 0.1 \text{ krad} = 10^{11} \cdot e \cdot \text{krad} = 1.602 \cdot 10^{-8} \text{krad},$$
$$1 \frac{\text{MeV}}{\text{mg}} = 1.602 \cdot 10^{-8} \text{krad}. \quad (\text{A.3})$$

It means that if we measure $\text{LET} \times F$ in $1 \frac{\text{MeV}}{\text{mg}}$, we should multiply it by factor $1.602 \cdot 10^{-8}$ to get krad.